

Random sequential adsorption of Pickering particles onto spherical emulsion droplet surfaces

*Original*

Random sequential adsorption of Pickering particles onto spherical emulsion droplet surfaces / Feng, Yi; Del Duca, Giulia; Buffo, Antonio; Simone, Elena. - In: PHYSICAL REVIEW. E. - ISSN 2470-0045. - 112:6(2025), pp. 1-18. [10.1103/hkc7-5dfm]

*Availability:*

This version is available at: 11583/3006554 since: 2026-01-15T11:12:00Z

*Publisher:*

American Physical Society - APS

*Published*

DOI:10.1103/hkc7-5dfm

*Terms of use:*

This article is made available under terms and conditions as specified in the corresponding bibliographic description in the repository

*Publisher copyright*

APS postprint/Author's Accepted Manuscript e postprint versione editoriale/Version of Record

This article appeared in PHYSICAL REVIEW. E, 2025, 112, 6, and may be found at <http://dx.doi.org/10.1103/hkc7-5dfm>.  
Copyright 2025 American Physical Society

(Article begins on next page)

1       **Random sequential adsorption of Pickering particles onto**  
2                   **spherical emulsion droplet surfaces.**

3               Yi Feng, Giulia Del Duca, Antonio Buffo, and Elena Simone\*

4                   *Department of Applied Science and Technology,*

5                           *Politecnico di Torino, Torino, Italy.*

6                                   (Dated: November 7, 2025)

# Abstract

Pickering emulsions are attracting growing attention as carriers of active ingredients or micro-nutrients in pharmaceutical and food applications, due to their high stability and low toxicity. The adsorption process of Pickering particles significantly affects emulsion properties and can be described using the random sequential adsorption (RSA) approach. While most studies focus on small, amorphous, spherical particles, the common use of elongated, crystalline, micron-sized particles in Pickering emulsions makes it necessary to consider the curvature and finite size of emulsion droplet surfaces to correctly understand and predict the interfacial adsorption behavior. The present study employs a Monte Carlo (MC) method to simulate the RSA process of both spherical and elongated micron-sized particles. Key factors such as particle polydispersity, emulsion droplet–particle size ratio, contact angle, and particle number are investigated. From the MC simulations, a new expression for the available surface function,  $ASF(\phi)$ , with coverage-dependent exponent is proposed. Based on this, generalized coverage evolution models are established using response surface methodology to relate RSA conditions to  $ASF(\phi)$  parameters. For spherical particles, jamming coverage and desorption energy under various conditions are reported. For capsule-shaped particles, an aspect ratio of  $\epsilon = 2$  is found to yield higher coverage and faster adsorption. The proposed  $ASF(\phi)$  expression outperforms existing fixed-exponent expressions. The generalized coverage evolution models show good agreement with MC testing simulations. The mean absolute percentage errors are less than 2.63% for spherical particles and 6.58% for elongated ones in the validation cases.

## 7 I. INTRODUCTION

8 Emulsions are widely used in pharmaceutical applications to protect active pharmaceu-  
9 tical ingredients (API) and to control their release [1]. Pickering emulsions, which are  
10 stabilized by solid particles, are attractive in pharmaceutical applications due to their high  
11 stability and low toxicity [2]. The properties of Pickering emulsions are closely linked to the  
12 adsorption process of the stabilizing particles, characterized by the coverage,  $\phi$ , defined as  
13 the fraction of the droplet surface area occupied by adsorbed particles. The low-coverage

---

\* Contact author: elena.simone@polito.it

14 behaviors of this adsorption process affect the size distribution of the emulsion droplets.  
15 The adsorbed particles stabilize the droplets, preserving the emulsion microstructure from  
16 coalescence and breakage. A faster adsorption process may lead to smaller droplets in a  
17 coalescence-dominated preparation process, but larger ones in a breakage-dominated pro-  
18 cess [3, 4]. Additionally, the asymptotic behaviors, which are the behaviors near the jamming  
19 state where no more particles can be adsorbed at the interface, affect the emulsion stability  
20 and eventually the API release rate. A higher jamming coverage,  $\phi_j$ , increases the total des-  
21 orption free energy of the Pickering particles, and thus enhances the stability of Pickering  
22 emulsions [5]. Regarding the release of the API, it is a diffusion process that depends on  
23 the size and particle coverage of emulsion droplets. Therefore, a thorough understanding  
24 of the adsorption process from both low-coverage and asymptotic perspectives is essential  
25 to design Pickering emulsions with desired microstructural properties for encapsulation and  
26 controlled release of APIs.

27 Depending on their physicochemical properties, Pickering particles may experience the  
28 short-range attraction and long-range repulsion [6]. As a result, the particles adsorbed at  
29 the interface of emulsion droplets can organize into various packing structures, including  
30 ordered arrangements [7], disordered arrangements [8, 9], or a combination of both [10]. In  
31 our previous experiments [11], curcumin crystals were used to stabilize water-in-oil Pickering  
32 emulsions. A disordered arrangement of elongated particles was observed on the droplet  
33 surfaces, as shown in FIG. 1, which can be attributed to the isotropic curvature of spherical  
34 emulsion droplets [12]. This study focuses on such disordered particle packings, which can be  
35 modeled using the random sequential adsorption (RSA) approach [13]. In the RSA model,  
36 particles arrive sequentially and attempt to adsorb at random locations on the surface [14].  
37 A particle is adsorbed only if it does not overlap with any previously adsorbed particles,  
38 and once adsorbed, it remains fixed in place.

39 The RSA problem has been extensively investigated in the literature. When particles  
40 are small enough compared to the droplet, the adsorbing interfaces can be regarded as  
41 planes [5]. Consequently, particles can be simplified to two-dimensional (2D) shapes, while  
42 adsorbing surfaces can be simplified to a sufficiently large planar area with periodic boundary  
43 conditions [15]. Based on this simplification, the RSA of particles with various shapes has  
44 been studied, including discs [16], squares [14], rectangles [17], discorectangles [18], ellipses  
45 [18, 19], polygons [20], rounded polygons [21], and other irregular shapes [22]. Different

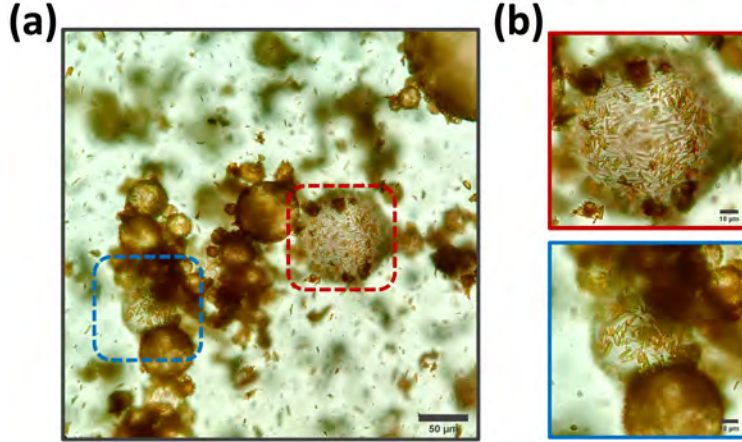


FIG. 1. Optical microscopy image of (a) water-in-oil emulsion droplets stabilized by elongated curcumin crystals, and (b) zoomed-in views showing the disordered arrangement of the crystals at the droplet interfaces. Brightness and contrast of the image were adjusted using Fiji software.

46 particle shapes typically result in varying jamming coverages and patterns.

47 Besides particle shape, other factors influencing the RSA process have been investigated.  
 48 For particles with anisotropic shapes, their orientations and aspect ratios significantly affect  
 49 both the low-coverage and asymptotic behaviors [23, 24]. For example, Ref. [25] found that  
 50 the jamming coverage of aligned discrectangle particles gradually increases with the aspect  
 51 ratio  $\epsilon$  to a maximum value of  $\phi_j = 0.5589$ . Meanwhile, the jamming coverage of unoriented  
 52 particles first increases and then decreases with  $\epsilon$ . A maximum  $\phi_j = 0.583 \pm 0.004$  was found  
 53 at  $\epsilon = 1.46$ . Moreover, as polydisperse Pickering particles are widely adopted in industry,  
 54 the effect of particle polydispersity on the RSA process has been explored in the literature.  
 55 Particles with binary [26], uniform [27], power-law [28], and Gaussian [29] size distributions  
 56 were investigated. Polydispersity was found to increase the jamming coverage because it  
 57 introduces smaller particles that can occupy the spaces among the larger previously adsorbed  
 58 ones [30].

59 The asymptotic and low-coverage behaviors are central topics in the RSA problem. The  
 60 asymptotic behaviors have been found to follow a power law given by:

$$\phi_j - \phi(n) \sim n^{-1/d}, \quad (1)$$

61 where  $\phi_j$  is the jamming coverage,  $\phi(n)$  is the coverage after  $n$  attempts of particle adsorption,  
 62  $d$  is a constant that depends on the shape and orientation of particles. Eq. (1) holds in the

vicinity of the jamming state, i.e., at a large  $n$ . Ref. [14] reported  $d = 2$  for disks and Ref. [31] found  $d = 3$  for anisotropic shapes. Consequently, Eq. (1) can be used to estimate  $\phi_j$  by extrapolating the results of experiments or simulations [13, 32].

In addition to the extrapolation method, the jamming coverage can be obtained using the concept of an exclusion zone. The exclusion zone of an adsorbed particle is the area in which no other particle can be placed because it overlaps with the adsorbed one [32, 33]. The area available for adsorption is tracked by recording changes in exclusion zones. Particles are continuously adsorbed to the available area until no available area is left, namely, the jamming state. Ref. [34] divided the adsorbing surface into voxels and used them to approximate the available area. They obtained the jamming coverages of different polygons. Ref. [35] and Ref. [18] adopted the voxel method with a different criterion from that of Ref. [34] to exclude unavailable voxels. They obtained the jamming coverages of rectangles, discorectangles, and ellipses.

For the low-coverage behaviors, the key quantity is the coverage change rate,  $d\phi/dt$ . Ref. [36] related  $d\phi/dt$  to the available surface function ( $ASF(\phi)$ ), which represents the probability of successful adsorption at coverage  $\phi$ . They derived an exact expansion for  $ASF(\phi)$  based on geometric and statistical considerations for the RSA of disks on a plane, and achieved good accuracy with the first several terms. Ref. [37, 38] developed an analogous approach for the lattice RSA, while Ref. [39] extended this method to anisotropic particles, and proposed two polynomial expressions for  $ASF(\phi)$ . Ref. [40] modified the polynomials for  $ASF(\phi)$  to make it consistent with Eq. (1). Ref. [41] adopted a fourth-order polynomial to fit their numerical results. Ref. [42] coupled  $ASF(\phi)$  with diffusion, particle-wall interactions, and external forces and proposed a generalized coverage evolution model. Moreover,  $d\phi/dt$  expressed using  $t$  and  $(\phi_j - \phi(t))$  with different exponents have been proposed [43–45].

The above studies provide valuable insights into the adsorption process of Pickering particles and are of great importance for the production of Pickering emulsions. It should be noted that most of these studies simplify the RSA process to two dimensions and neglect the effects of the curvature and the finite size of emulsion droplet surfaces. Such simplifications are reasonable for particles of sufficiently small sizes, such as those in the nanometer range. However, crystalline microparticles have received increasing attention for emulsion stabilization [46]. Micron-sized, crystalline particles obtained by milling or shearing starches and cellulose [47] are widely adopted due to their high availability and low cost. Alternatively,

95 polyphenol crystals can be used as Pickering particles due to their added health effects; as  
96 an example, our previous work has demonstrated the use of curcumin crystals as Pickering  
97 stabilizers of water-in-oil emulsions [11]. These larger particles lead to smaller emulsion  
98 droplet–particle size ratios, ranging from 10 to 100 [3, 48–52]. Under such conditions, the  
99 curvature and finite size of spherical droplet surfaces cannot be ignored. Despite their rele-  
100 vance, studies on the RSA of particles on curved surfaces remain limited [53–56].

101 To address these current gaps in knowledge, this study has two complementary aims: the  
102 first is to quantify the RSA behaviors (both low-coverage and asymptotic) of micron-sized  
103 spherical and capsule-shaped particles on the curved, finite emulsion droplet surfaces; and  
104 the second is to present a research framework for developing a generalized coverage evo-  
105 lution model to efficiently predict the RSA process across varied conditions. Therefore, a  
106 Monte Carlo method accounting for the curvature and finite-size effects is developed to sim-  
107 ulate the RSA process of both spherical and elongated (capsule-shaped) particles. Various  
108 influencing factors, such as particle polydispersity and average particle size, are explored.  
109 Particularly, based on the work of Ref. [18] and Ref. [35], we extend the voxel method to  
110 polydisperse spherical particles to accurately estimate their jamming coverage. With the  
111 MC results, the available surface function  $ASF(\phi)$  can be evaluated. We then propose a  
112 new expression for  $ASF(\phi)$  with a coverage-dependent exponent to better capture the ad-  
113 sorption process and compare it with fixed-exponent forms [39]. Finally, response surface  
114 methodology (RSM) is used to relate the fitted  $ASF(\phi)$  parameters to the influencing fac-  
115 tors, yielding a generalized coverage evolution model that predicts coverage evolution over  
116 diverse conditions without the need to run costly MC simulations. The novelty of this work  
117 lies in explicitly treating curvature and finite-surface effects of emulsion droplet surfaces and  
118 the RSM-based generalized coverage evolution model for RSA process.

119 The resulting jamming coverage data for spherical particles are directly relevant to mod-  
120 eling API release from Pickering emulsions. In addition, the generalized coverage evolution  
121 model provides a practical tool for predicting the RSA process across varied conditions,  
122 aiding the design and production of emulsions stabilized by micron-sized crystals.

123 The manuscript is organized as follows: Section II introduces the geometric relationships  
124 between Pickering particles and spherical emulsion droplet surfaces, the MC method used  
125 for the RSA process, and the generalized coverage evolution model. Section III focuses on  
126 the RSA process and the corresponding generalized coverage evolution model for spherical

127 particles, while Section IV addresses those for capsule-shaped particles. Conclusions are  
 128 drawn in Section V.

## 129 II. METHODOLOGY

### 130 A. Geometric relationships

131 When the emulsion droplet–particle size ratio is small or moderate, such as between 10 to  
 132 100, the curvature and finite size of the emulsion droplet surface cannot be neglected. These  
 133 effects can be incorporated by considering the geometric relationships between particles and  
 134 droplets.

#### 135 1. Spherical particles

136 The curvature of a spherical droplet surface influences the relative position of adsorbed  
 137 particles through the contact angle. FIG. 2(a) shows the geometric relationships between  
 138 a spherical particle and a spherical droplet. The emulsion droplet–particle center distance,  
 139  $l_{dp}$ , is determined by the radius of both the droplet and particle,  $r_d$  and  $r_p$ , and the contact  
 140 angle,  $\theta$ , as described by the following equation [57, 58]:

$$l_{dp} = r_d \cos \beta - r_p \cos(\beta + \theta), \quad (2)$$

141 where  $\theta \in [0, \pi]$ , and the half-apex angle of the droplet cap,  $\beta$ , is calculated as:

$$\beta = \arctan \left( \frac{r_p/r_d \sin \theta}{1 - r_p/r_d \cos \theta} \right). \quad (3)$$

142 As shown in Fig. 2(a),  $\beta$  also represents the angle between  $\gamma_{ow}$  and a horizontal reference  
 143 plane (a flat surface simplifying the spherical droplet surface as illustrated by the dashed  
 144 line). Therefore,  $\beta$  measures the effect of the droplet surface curvature. For a fixed contact  
 145 angle,  $\beta$  approaches zero when the emulsion droplet–particle radius ratio approaches infinity,  
 146  $r_d/r_p \rightarrow \infty$ , namely, the spherical droplet surface can be approximated by a plane when  
 147 particles are sufficiently small [5]. When  $r_d/r_p$  is small or moderate (i.e., between 10 and  
 148 100), the increased  $\beta$  makes it necessary to consider the effect of curvature.

149 The coverage of a single spherical particle,  $\phi_{p,shp}$ , can be calculated as [53]:

$$\phi_{p,shp} = \sin^2 \left( \frac{\beta}{2} \right). \quad (4)$$

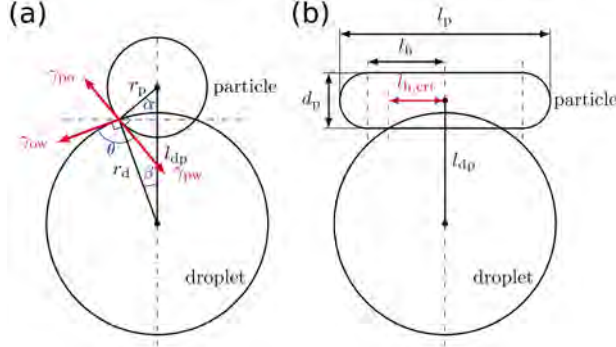


FIG. 2. Geometric relationship between (a) spherical particle and (b) capsule-shaped particle and a spherical droplet.  $\gamma_{po}$ ,  $\gamma_{pw}$ , and  $\gamma_{ow}$  are surface tensions. This is a water-in-oil emulsion.

150 For polydisperse particles, the jamming coverage can be calculated as  $\phi_j = \sum_{i=1}^{N_{ad,j}} \sin^2(\beta_i/2)$ ,  
 151 where  $N_{ad,j}$  is the number of adsorbed particles at the jamming state.

152 Additionally, the free energy of particle desorption at the jamming state,  $\Delta G_d$ , measures  
 153 the stability of the Pickering emulsions [5]. A higher  $\Delta G_d$  implies that the adsorbed particles  
 154 require more energy to desorb from the emulsion droplets, and thus the Pickering emulsions  
 155 are more stable. For the spherical particles and droplets,  $\Delta G_d$  can be calculated as [5, 57]:

$$\Delta G_d = \begin{cases} \gamma_{ow}(A_c - A_{po} \cos \theta), & 0^\circ \leq \theta < 90^\circ \\ \gamma_{ow}(A_c + A_{pw} \cos \theta), & 90^\circ \leq \theta \leq 180^\circ \end{cases}, \quad (5)$$

156 where  $A_c = 4\pi r_d^2 \phi_j$  is the area of the oil-water interface occupied by the adsorbed parti-  
 157 cles,  $A_{po} = \sum_{i=1}^{N_{ad,j}} 4\pi r_{p,i}^2 (1 - \sin^2(\alpha_i/2))$  is the total area of particle-oil interface,  $A_{pw} =$   
 158  $\sum_{i=1}^{N_{ad,j}} 4\pi r_{p,i}^2 \sin^2(\alpha_i/2)$  is the total area of particle-water interface, and  $\alpha_i = \pi - \theta - \beta_i$  is  
 159 the half-apex angle of the particle cap. In the following sections,  $\Delta G_d$  is normalized by  
 160 the thermal energy  $k_B T$ , where  $k_B$  is the Boltzmann constant and  $T = 298.15$  K is the  
 161 temperature.

## 162 2. Capsule-shaped particles

163 Capsule-shaped particles are characterized by their aspect ratio,  $\epsilon$ , defined as  $\epsilon = l_p/d_p$ ,  
 164 where  $l_p$  is the particle length and  $d_p$  is the diameter, as shown in FIG. 2(b). The contact  
 165 area between capsule-shaped particles and spherical droplets can be complex, as the droplet  
 166 surface may deform to satisfy the contact angle along the entire contact line [59, 60]. In

167 this study, however, the droplet surface is assumed to remain undeformed and perfectly  
 168 spherical upon adsorption. The contact angle is assumed to be satisfied only at the central  
 169 cross-section of the particle. Under this assumption, the emulsion droplet–particle center  
 170 distance,  $l_{\text{dp}}$ , is calculated in the same manner as described in Section II A 1. The half length  
 171 of the cylindrical part can be defined as:

$$l_{\text{h}} = \frac{l_{\text{p}} - d_{\text{p}}}{2}. \quad (6)$$

172 Then, there is a critical value,  $l_{\text{h,crt}}$ , equal to:

$$l_{\text{h,crt}} = \sqrt{r_{\text{d}}^2 - (l_{\text{dp}} - r_{\text{p}})^2}, \quad (7)$$

173 so that if  $l_{\text{h}} \geq l_{\text{h,crt}}$ , the semi-spherical parts are completely outside the droplet, and if  
 174  $l_{\text{h}} < l_{\text{h,crt}}$ , the semi-spherical parts are partially inside the droplet. The corresponding  
 175 critical aspect ratio can be calculated as  $\epsilon_{\text{crt}} = (2l_{\text{h,crt}} + d_{\text{p}})/d_{\text{p}}$ .

176 The coverage of a single capsule-shaped particle,  $\phi_{\text{p,cap}}$ , can be calculated as:

$$\phi_{\text{p,cap}} = \frac{S_{\text{d,p}}}{S_{\text{d}}} = \frac{\int_{\vartheta_1}^{\vartheta_2} \int_{\varphi_1(\vartheta)}^{\varphi_2(\vartheta)} r_{\text{d}}^2 \sin \vartheta \, \text{d}\varphi \, \text{d}\vartheta}{4\pi r_{\text{d}}^2}, \quad (8)$$

177 where  $S_{\text{d,p}}$  is the droplet surface area covered by the particle, and  $S_{\text{d}}$  is the droplet surface  
 178 area. The value of  $S_{\text{d,p}}$  is determined through numerical integration, with the procedure  
 179 detailed in Section S1 of the Supplemental Material [61].

## 180 B. Monte Carlo method

181 The RSA process of particles can be simulated using the MC method. At each adsorp-  
 182 tion attempt, a particle, with a random size and at a random location constrained by the  
 183 geometric relationships defined in Section II A, is generated. Its overlap with previously  
 184 adsorbed particles is then examined. Based on the result, the particle is either adsorbed  
 185 or discarded. This MC simulation yields the evolution of the surface coverage  $\phi$  and the  
 186 number of adsorbed particles  $N_{\text{ad}}$  as a function of the number of attempts  $n$ . The simulation  
 187 procedure is detailed in the following part.

189 This study investigates the effect of particle polydispersity on the adsorption process. The  
 190 radii of a distribution of spherical particles,  $r_p$ , are assumed to follow a normal function,  
 191  $\mathcal{N}(\mu, \sigma^2)$ , truncated to the range  $[\mu - 3\sigma, \mu + 3\sigma]$ . The parameters  $\mu$  and  $\sigma$  are equal to  
 192 the mean ( $\mu_X$ ) and the standard deviation ( $\sigma_X$ ) of the distribution, respectively. However,  
 193 it should be emphasized that the methodology is not limited to a normal distribution, and  
 194 it can be easily extended to other particle size distribution functions. Two approaches are  
 195 employed to generate particle radii:

- 196 1. Infinite particle method: New radii are continuously generated from the truncated  
 197 normal distribution;
- 198 2. Finite particle method: A total of  $N_p$  particle radii are first generated from the trun-  
 199 cated normal distribution to form a finite pool. At each attempt, a particle with a  
 200 specific radius is randomly selected from this pool. If the corresponding particle is  
 201 successfully adsorbed, the radius is removed from the pool; otherwise, it is returned  
 202 for future attempts.

203 In the infinite particle method, adsorption does not affect the available particles for future  
 204 adsorption attempts, implying an infinite number of particles. This approach eliminates the  
 205 influence of particle number and is therefore used in the investigation of other influencing  
 206 factors, such as particle polydispersity and particle size. In contrast, the finite particle  
 207 method accounts for a limited number of particles, as in practical applications. This method  
 208 is mainly applied in the establishment of a generalized coverage evolution model.

209 To generate a random location for a spherical particle, a spherical coordinate system,  
 210  $(\varrho, \vartheta, \varphi)$ , with its origin at the droplet center, is adopted. According to the geometric  
 211 relationships in Section II A 1, the effect of surface curvature is incorporated by setting  
 212  $\varrho = l_{dp}$ , where  $l_{dp}$  is calculated using Eq. (2). Two additional random values,  $\vartheta$  and  $\varphi$ , are  
 213 then required to determine the particle's location. Since the droplet surface is continuous  
 214 and all locations are equally probable,  $\varphi$  is drawn from a uniform distribution  $\mathcal{U}[0, 2\pi]$ ,  
 215 and  $\vartheta$  is generated by sampling  $\cos \vartheta \sim \mathcal{U}[-1, 1]$ . This sampling method ensures uniform  
 216 distribution over the spherical surface.

217 The overlap between two spherical particles is checked by comparing the distance between

218 their centers with the sum of their radii. If the center-to-center distance is less than the  
219 sum, an overlap is detected and the new particle is discarded.

## 220 2. Capsule-shaped particles

221 For polydisperse capsule-shaped particles, a fixed aspect ratio  $\epsilon$  is specified. Two dis-  
222 tributions are adopted for particle length,  $l_p$ , in this study. One is the normal distribution  
223  $\mathcal{N}(\mu, \sigma^2)$ , truncated to the range  $[\mu - 3\sigma, \mu + 3\sigma]$ , with  $\mu = \mu_X$  and  $\sigma = \sigma_X$ . The other  
224 is the lognormal distribution  $\mathcal{L}(\mu, \sigma^2)$ , truncated to the range  $[\exp(\mu - 3\sigma), \exp(\mu + 3\sigma)]$   
225 with  $\mu = \ln\left(\mu_X^2/\sqrt{\mu_X^2 + \sigma_X^2}\right)$  and  $\sigma^2 = \ln(1 + \sigma_X^2/\mu_X^2)$ .  $\mu_X$  and  $\sigma_X$  are the mean and the  
226 standard deviation of the distributions, respectively.

227 As with spherical particles, two random numbers are used to determine the particle's  
228 position on the droplet surface. However, due to the anisotropic nature of capsule-shaped  
229 particles, orientation also influences the adsorption process. In our approach, the orientation  
230 is restricted to lie within the plane tangent to the spherical surface passing through the  
231 particle's center. Accordingly, an additional random angle  $\varpi$ , sampled from a uniform  
232 distribution  $\mathcal{U}[0, 2\pi]$ , is introduced to specify the particle's orientation.

233 To examine the overlap between two capsule-shaped particles, each is modeled as a line  
234 segment with rounded ends. The shortest distance between the segments is computed and  
235 compared with the sum of their radii [62] to determine whether an overlap occurs.

## 236 3. Additional simulation details

237 In this study, each simulation ran for  $n = 1 \times 10^8$  adsorption attempts. This number was  
238 sufficiently large to reach a high coverage, but not enough to ensure reaching the jamming  
239 state. As mention previously,  $\phi$  increases toward  $\phi_j$  following the power law,  $\phi_j - \phi(n) \sim$   
240  $n^{-1/d}$ . Approaching the jamming state, the number of failed attempts between two successive  
241 successful adsorption events grows rapidly, making the MC simulations computationally  
242 infeasible.

243 To address this problem, a voxel method for polydisperse, spherical particles is developed  
244 based on the work of Ref. [35] and Ref. [18]. In the developed method, each voxel has  
245 three dimensions: the first two discretize the droplet surface, and the third discretizes the

246 particle radius. The new method can efficiently obtain the jamming coverages of polydisperse  
247 spherical particles. Details of the developed voxel method are provided in Section S2 of the  
248 Supplemental Material [63]. For spherical particles, the voxel method is applied based on the  
249 results of the MC simulations to obtain the coverage and the number of adsorbed particles  
250 at the jamming state.

251 For capsule-shaped particles, the voxel method becomes more challenging due to the addi-  
252 tional complexity introduced by particle anisotropy in three dimensions. Ref. [18] proposed  
253 a voxel method for a two-dimensional problem: the RSA of discorectangles (2D capsules) on  
254 a plane. However, its extension to three-dimensional particles is non-trivial. Consequently,  
255 the RSA of capsule-shaped particles is investigated using only the MC method in this study.

256 When the finite particle method (Section II B 1) is used, the physical time,  $t$ , can be  
257 estimated by mapping adsorption attempts to particle–emulsion droplet collisions. This  
258 mapping is necessary to study the effect of particle concentration, because expressing cover-  
259 age evolution as  $\phi(n)$  assumes a concentration-independent attempt rate and thus obscures  
260 the influence of particle concentration. To this end, each adsorption attempt is interpreted  
261 as a particle–emulsion droplet collision, and the corresponding time interval is computed us-  
262 ing a collision kernel that specifies the collision frequency [4]. In principle, turbulent kernels  
263 are most appropriate, since Pickering emulsions are generally prepared in turbulent flows  
264 induced by high shear mixers [11]. However, they require empirical constants or turbulence  
265 fields, introducing uncertainty. For simplicity, we adopt the Brownian collision kernel, which  
266 depends only on material properties and temperature. Accordingly, this time mapping is in-  
267 tended to illustrate the effect of particle concentration on the RSA process, not to reproduce  
268 experimental time scales. Detailed equations are provided in Section S3 of the Supplemental  
269 Material [64] (see also references [65–68] therein).

270 To ensure statistical reliability of the MC simulations, the convergence with respect to  
271 the number of simulations,  $N_{\text{sim}}$ , is analyzed (detailed in Section S3 of the Supplemental  
272 Material [64]). Satisfactory convergence can be obtained for  $N_{\text{sim}} \geq 25$ . Considering compu-  
273 tational efficiency, most simulations in this study are performed with  $N_{\text{sim}} = 50$ . However,  
274 when constructing the generalized coverage evolution model for capsuled-shaped particles in  
275 Section IV C,  $N_{\text{sim}} = 25$  is adopted to reduce computational costs while maintaining accept-  
276 able accuracy. Throughout this work, standard deviations are generally reported alongside  
277 mean values by error bars. However, in most cases, the deviations are too small to be visible

278 in the figures.

### 279 C. Generalized coverage evolution model

280 The coverage evolution during the RSA process can be modeled with the help of the  
 281 available surface function,  $ASF(\phi)$  [13, 39]. This function quantifies the probability of  
 282 successful adsorption at a given surface coverage  $\phi$ . However, the parameters of  $ASF(\phi)$   
 283 may vary with influencing factors of the RSA process, such as particle polydispersity and  
 284 emulsion droplet–particle size ratio. To establish a generalized coverage evolution model  
 285 applicable across varied conditions, the response surface methodology is adopted to relate  
 286 the influencing factors to the parameters of  $ASF(\phi)$ .

#### 287 1. Available surface function

288 The coverage change rate concerning the number of adsorption attempts can be written  
 289 as [39]:

$$\frac{d\phi}{dn} = \bar{\phi}_p(\phi)ASF(\phi), \quad (9)$$

290 where  $\bar{\phi}_p(\phi)$  is the average coverage provided by a single particle at the coverage of  $\phi$ .  
 291 For polydisperse particles,  $\bar{\phi}_p(\phi)$  decreases with increasing  $\phi$  because smaller particles more  
 292 easily fill the space between previously adsorbed particles. For simplicity, a constant  $\bar{\phi}_p$   
 293 based on the mean particle size is used in this study. Then, we have:

$$ASF(\phi) = \frac{1}{\bar{\phi}_p} \frac{d\phi}{dn}, \quad (10)$$

294 where  $d\phi/dn$  can be obtained from the MC simulations [41].

295 Ref. [39] proposed two fitting expressions for  $ASF(\phi)$ , which cover both the low-coverage  
 296 and the asymptotic behaviors, referred to here as Fit 1 and Fit 2, respectively:

$$ASF_1(x) = (1-x)^4(1+c_1x+c_2x^2), \quad (11)$$

$$ASF_2(x) = \frac{(1-x)^4}{(1+d_1x+d_2x^2)}, \quad (12)$$

298 where  $x = \phi/\phi_j$ ,  $\phi_j$ ,  $c_1$ ,  $c_2$ ,  $d_1$ , and  $d_2$  are fitting parameters. Additionally, we propose a new  
 299 expression (denoted as Fit 3) purely from fitting considerations as:

$$ASF_3(y) = e_1y^{e_2(1+\exp(e_3y))}, \quad (13)$$

300 where  $y = \phi_j - \phi$ ,  $\phi_j$ ,  $e_1$ ,  $e_2$ , and  $e_3$  are fitting parameters. Compared with Fit 1 and  
 301 Fit 2, Fit 3 adopted a coverage-dependent exponent, which is more flexible to deal with the  
 302 adsorption of polydisperse or anisotropic particles.

303 Once  $ASF(\phi)$  is known, the coverage evolution model can be written as:

$$\phi(n + \Delta n) = \phi(n) + \bar{\phi}_p ASF(\phi(n)) \Delta n, \quad (14)$$

304 where  $\phi(0) = 0$ , and  $\Delta n$  is the step. Eq. (14) can be solved using a forward Euler method.

## 305 2. Response surface methodology

306 The response surface methodology is a statistical technique used to develop an adequate  
 307 functional relationship between a response of interest,  $y$ , and a number of associated input  
 308 variables denoted by  $x_i$  [69]. In this study, a second-order response surface model is adopted  
 309 to link influencing factors to  $ASF(\phi)$  parameters, which can be expressed as [70]:

$$y = \beta_0 + \sum_{i=1}^N \beta_i x_i + \sum_{i=1}^N \beta_{ii} x_i^2 + \sum_{i=1}^{N-1} \sum_{j=i+1}^N \beta_{ij} x_i x_j + \epsilon_{\text{RSM}}, \quad (15)$$

310 where  $y$  is the response ( $ASF(\phi)$  parameters),  $x_i$  are the input variables (influencing factors  
 311 of the RSA process), such as particle polydispersity or emulsion droplet–particle size ratio,  
 312  $\beta_0$ ,  $\beta_i$ ,  $\beta_{ii}$ , and  $\beta_{ij}$  are the regression coefficients to be estimated,  $N$  is the number of input  
 313 variables, and  $\epsilon_{\text{RSM}}$  is a random error term with a zero mean.

314 To construct the generalized coverage evolution model, the Latin hypercube sampling  
 315 (LHS) method [70] is employed to generate combinations of influencing factors as input  
 316 conditions for the MC simulations. The resulting simulation data form the training dataset,  
 317 which is first used to fit the parameters of  $ASF(\phi)$  [71]. Each fitted parameter is then  
 318 regressed against the training conditions to develop a generalized coverage evolution model  
 319 applicable across varied conditions. To validate the constructed model, the central compos-  
 320 ite design (CCD) [70] is employed to generate a separate set of input conditions distinct  
 321 from those in the training dataset. Model accuracy is evaluated using the coefficient of  
 322 determination ( $R^2$ ) [70] and the mean absolute percentage error (MAPE) [72]. The detailed  
 323 construction procedure is provided in the Supplemental Material (Section S4 [73]).

324 It is important to emphasize that the generalized coverage evolution model is purely em-  
 325 pirical. Although it does not capture the underlying physics of the RSA process, it provides

326 a practical approximation that describes the relationships between key influencing factors  
 327 and the  $ASF(\phi)$  parameters. Furthermore, the proposed framework is general and adapt-  
 328 able: it can be readily extended to Pickering particles with different properties by updating  
 329 the MC simulation setups (i.e., the representative samples used in applying response surface  
 330 methodology) and, if necessary, adjusting the fitting expression of  $ASF(\phi)$ .

### 331 III. ADSORPTION OF SPHERICAL PARTICLES

332 In this section, the RSA process of spherical Pickering particles was investigated from  
 333 both the asymptotic and kinetic perspectives. The effects of key influencing factors are  
 334 analyzed, and a generalized coverage evolution model is developed.

#### 335 A. Infinite particles

336 The effects of polydispersity, emulsion droplet–particle radius ratio, and contact angle  
 337 on the RSA process of Pickering particles are investigated in this work. The evolutions  
 338 of the number of adsorbed particles,  $N_{\text{ad}}$ , and the coverage,  $\phi$ , are obtained from the MC  
 339 simulations. The jamming coverage,  $\phi_j$ , and the free energy of particle desorption,  $\Delta G_d$ , are  
 340 obtained using the voxel method. TABLE I summarizes the setups for the simulations. The  
 341 polydispersity is measured by the coefficient of variation defined as  $CV = \sigma_X/\mu_X$ . Higher  
 342  $CV$  gives a wider particle size distribution, namely, higher polydispersity.

#### 343 1. Effect of polydispersity

344 FIG. 3 shows the effect of polydispersity on the RSA process. FIG. 3(a) and FIG. 3(b)  
 345 present the variations of the jamming coverage  $\phi_j$  and the normalized free energy of par-  
 346 ticle desorption  $\Delta G_d/k_B T$  with the coefficient of variation  $CV$ . The mean values and the  
 347 standard deviations are represented by circles and error bars, respectively. The small stan-  
 348 dard deviations indicate that the number of MC simulations is sufficiently large to yield  
 349 reliable results. It can be observed that both  $\phi_j$  and  $\Delta G_d$  increase with  $CV$ . According to  
 350 Eq. (5), the second term,  $A_{\text{pw}} \cos \theta$ , vanishes when  $\theta = 90^\circ$ . Consequently,  $\Delta G_d$  increases  
 351 proportionally with  $\phi_j$ . Additionally,  $\Delta G_d \gg k_B T$ , indicating a desorption barrier far above

TABLE I. The MC simulation setups for spherical particles.

Variables <sup>a</sup>	Polydispersity	Radius ratio	Contact angle	Particle number <sup>b</sup>
$\mu_X$ ( $\mu\text{m}$ )	1	1	1	1
$CV$ (-)	0, 0.05, 0.1, 0.2	0.1	0.1	0.1
$r_d/r_p$ (-)	40	20, 40, 100	40	40
$\theta$ ( $^\circ$ )	90	90	90, 120, 150	90
$m_p/m_d$	$\infty^c$	$\infty$	$\infty$	0.10, 0.41, 1.63, 6.53

<sup>a</sup>  $\mu_X$  is the mean particle size,  $CV = \sigma_X/\mu_X$  is the coefficient of variation of the size distribution,  $r_d$  and  $m_d$  are the emulsion droplet radius and mass,  $r_p$  and  $m_p$  are the particle radius and mass, and  $\theta$  is the contact angle.

<sup>b</sup> Particle number measured by the particle–emulsion droplet mass ratio  $m_p/m_d$ .

<sup>c</sup>  $m_p/m_d = \infty$  represents using the infinite particle method.

352 thermal energy and thus confirming the high stability of Pickering emulsions.

353 The effect of  $CV$  can be explained by the evolution of adsorbed particle size distribution  
 354 shown in FIG. 4. As adsorption proceeds, the distribution skews toward smaller sizes. At  
 355 the jamming state ( $n = \infty$ ), the share of small particles has increased significantly. This is  
 356 because the small particles can further fill the space between the adsorbed large particles  
 357 [30]. Increasing  $CV$  introduces particles with smaller sizes, which are further adsorbed as  
 358 shown in FIG. 4(b), and cause the increment in  $\phi_j$  and  $\Delta G_d$ .

359 FIG. 3(c) and FIG. 3(d) present the effect of  $CV$  on the evolution of  $N_{ad}$ , and  $\phi$ . When  
 360  $n \leq 10^4$ , the trends for different  $CV$  are close. At the beginning of the adsorption process,  
 361 the droplet surface is empty. The probability of successful adsorption is close to 1, so  $N_{ad}$   
 362 evolutions are almost identical. The size distributions of adsorbed particles are close to the  
 363 initial distributions, as shown in FIG. 4. As a result,  $\phi$  evolutions are also close. Once the  
 364 droplet has adsorbed sufficient particles, the probability of successful adsorption decreases  
 365 and closely depends on the size of incoming particles. Consequently, larger  $CV$  values mean  
 366 that there are smaller particles that can fill the space between the larger previously adsorbed  
 367 ones. This gives a significant increment in  $N_{ad}$  when  $n > 1 \times 10^4$ . At the same time,  $\phi$   
 368 increases moderately because of the smaller sizes of the newly adsorbed particles.

369 In addition, when the number of attempts reaches  $n = 1 \times 10^8$ , the coverage for  $CV = 0$

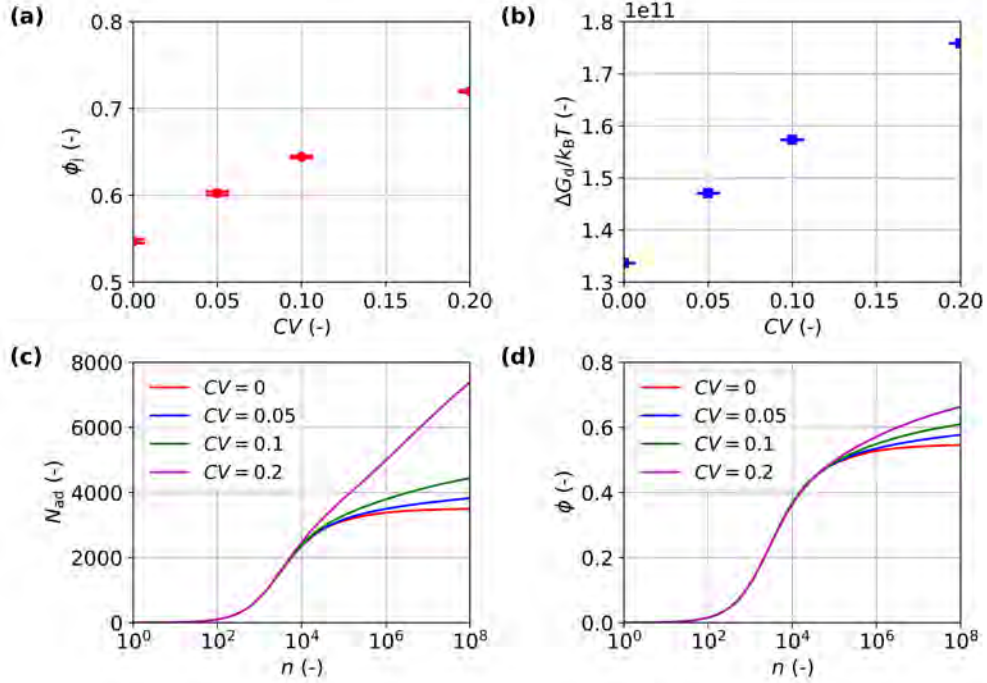


FIG. 3. The effect of polydispersity,  $CV$ , on (a)  $\phi_j$ , (b)  $\Delta G_d/k_B T$ , (c) evolution of  $N_{ad}$ , and (d) evolution of  $\phi$ .

370 reaches 99.6% of  $\phi_j$ , while that for  $CV = 0.2$  reaches 93.7% of  $\phi_j$ . This indicates that  $1 \times 10^8$   
 371 attempts are sufficient to approach a near-jamming state.

## 372 2. Effect of emulsion droplet–particle radius ratio

373 FIG. 5 illustrates the effect of the emulsion droplet–particle radius ratio,  $r_d/r_p$ , on the  
 374 RSA process. As shown in FIG. 5(a), both the mean values and the standard deviations of  $\phi_j$   
 375 decrease with increasing  $r_d/r_p$ . The larger variations in  $\phi_j$  observed for smaller droplets are  
 376 not caused by the limited number of simulations (see FIG. S5 in the Supplemental Material  
 377 [64]) but are intrinsic to the system, reflecting a finite-size effect. When  $r_d/r_p = 20$ , the  
 378 droplet can adsorb only a small number of particles, which is insufficient to average out  
 379 the random fluctuations arising from particle size polydispersity and stochastic adsorption  
 380 events. In contrast, when  $r_d/r_p \geq 40$ , the larger number of adsorbed particles effectively  
 381 suppresses these fluctuations, resulting in smaller variations in  $\phi_j$ .

382 Furthermore, it can be observed that in the production of Pickering emulsions with a  
 383 sufficient quantity of particles, droplets of varying sizes tend to reach comparable levels

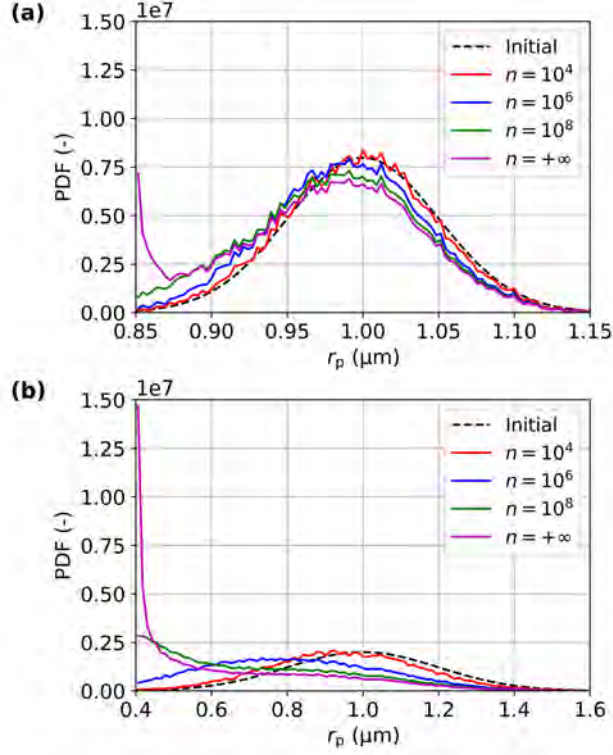


FIG. 4. Evolution of adsorbed particle size distribution of (a)  $CV = 0.05$  and (b)  $CV = 0.2$ .  $n$  is the number of attempts.  $n = \infty$  represents the jamming state obtained by the voxel method.

384 of coverage. This information simplifies the estimation of the API release rates because  
 385 the variations in jamming coverage due to droplet polydispersity are negligible. FIG. 5(b)  
 386 presents an increasing  $\Delta G_d$ . According to Eq. (5),  $\Delta G_d$  is proportional to  $r_d^2$  when  $\theta$  is  $90^\circ$   
 387 and  $\phi_j$  is a constant.

388 The evolutions of  $N_{ad}$  and  $\phi$  are shown in FIG. 5(c) and FIG. 5(d). Larger droplets  
 389 ( $r_d/r_p = 100$ ) adsorb more particles and have a significantly larger  $N_{ad}$ . Their coverage  
 390 increases more slowly due to the large surface area. However, it finally reaches a jamming  
 391 coverage close to that of smaller droplets, as mentioned previously.

### 392 3. Effect of contact angle

393 FIG. 6 shows the effect of contact angle,  $\theta$ , on the RSA process. Both  $\phi_j$  and  $\Delta G_d$   
 394 decrease as  $\theta$  increases from  $90^\circ$  to  $150^\circ$ , as shown in FIG. 6(a) and FIG. 6(b). According  
 395 to Eq. (3), for a fixed  $r_d/r_p$ ,  $\beta$  reaches its maximum value when  $\theta_{mp} = \arccos(r_p/r_d)$ , which  
 396 corresponds to an angle smaller than  $90^\circ$ .  $\beta$  increases monotonically for  $0^\circ \leq \theta \leq \theta_{mp}$ ,

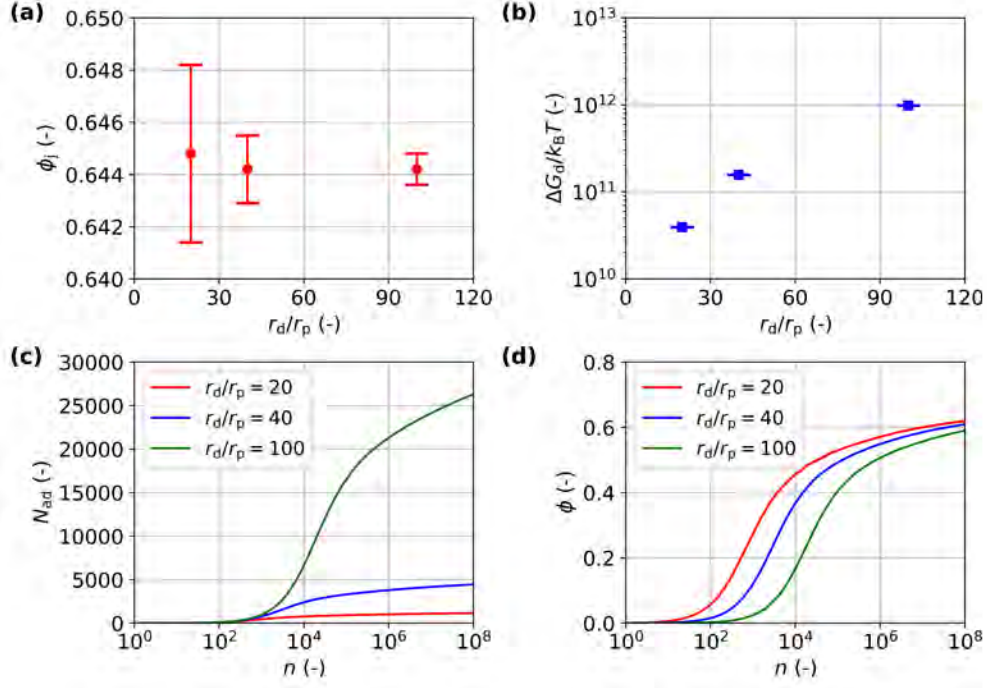


FIG. 5. The effect of emulsion droplet–particle radius ratio,  $r_d/r_p$ , on (a)  $\phi_j$ , (b)  $\Delta G_d/k_B T$ , (c) evolution of  $N_{ad}$ , and (d) evolution of  $\phi$ .

397 and decreases monotonically for  $\theta_{mp} \leq \theta \leq 180^\circ$ . Therefore, within the considered range,  
 398  $[90^\circ, 180^\circ]$ , the coverage provided by a single spherical particle,  $\phi_{p,sph}$ , decreases according to  
 399 Eq. (4). Meanwhile, the emulsion droplet–particle center distance,  $l_{dp}$ , increases slightly, as  
 400 given by Eq. (2). This creates additional space for particle adsorption, resulting in a modest  
 401 increase in  $N_{ad}$ , as shown in FIG. 6(c). However, this slight increase in  $N_{ad}$  is insufficient to  
 402 compensate for the decrease in  $\phi_{p,sph}$ . Consequently,  $\phi_j$  decreases as  $\theta$  increases from  $90^\circ$  to  
 403  $150^\circ$ , as illustrated in FIG. 6(d).

404 The decreasing trend of  $\Delta G_d$  is more significant than that of  $\phi_j$  because the second term  
 405 in Eq. (5),  $A_{pw} \cos \theta$ , becomes negative when  $\theta > 90^\circ$ . This finding supports the argument  
 406 of Ref. [47] that  $\theta$  should be between  $30^\circ$  and  $150^\circ$  to have a sufficient energy barrier to  
 407 prevent particle desorption.

## 408 B. Finite particles

409 The finite particle method is employed in this section to investigate the effect of Pickering  
 410 particle number and to develop a generalized coverage evolution model. The particle number

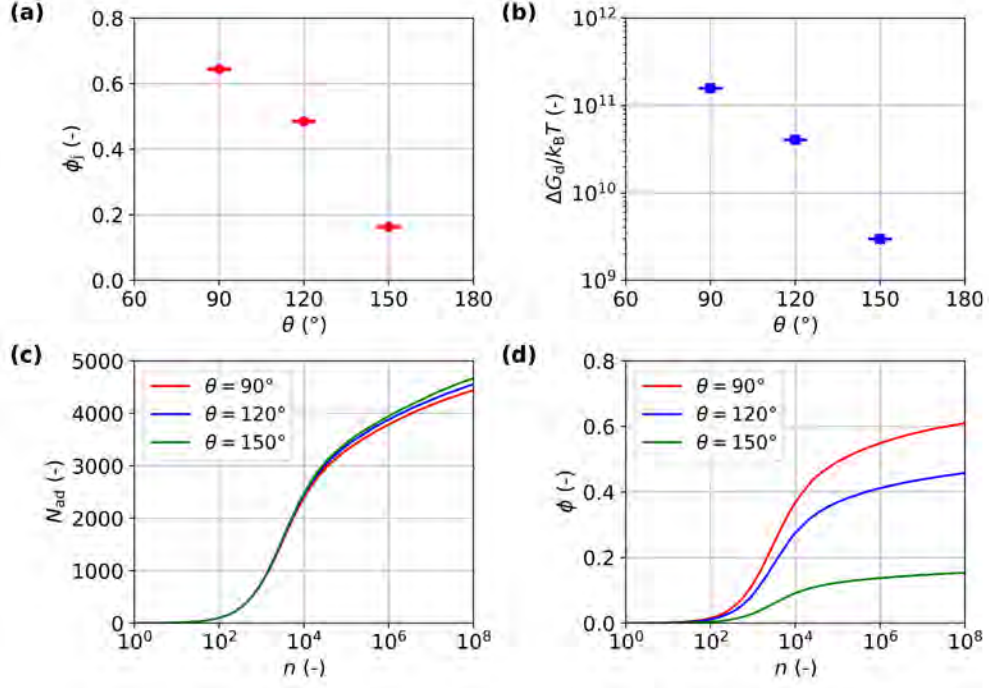


FIG. 6. The effect of contact angle,  $\theta$ , on (a)  $\phi_j$ , (b)  $\Delta G_d/k_B T$ , (c) evolution of  $N_{ad}$ , and (d) evolution of  $\phi$ .

411 is measured by the particle–emulsion droplet mass ratio,  $m_p/m_d$ , defined as:

$$\frac{m_p}{m_d} = \frac{N_p \rho_p r_p^3}{N_d \rho_d r_d^3}, \quad (16)$$

412 where  $N_d = 1$  is the droplet number, since we are considering the particle adsorption on  
 413 one droplet.  $\rho_p$  and  $\rho_d$  are the particle and droplet density, respectively. In the case of  
 414 water-in-oil emulsions stabilized by crystalline organic particles, it is reasonable to assume  
 415 that  $\rho_p/\rho_d = 1$  [11]. For polydisperse particles, the particle radius is calculated using the  
 416 third-order moments of the normal particle size distribution  $\mathcal{N}(\mu, \sigma^2)$  as  $r_p^3 = \mu^3 + 3\mu\sigma^2$ .

417 Furthermore, the Brownian collision kernel is adopted here to estimate the physical time  
 418  $t$ . The following parameters and conditions are specified: the temperature  $T = 298.15$  K,  
 419 the viscosity  $\mu_c = 0.03$  Pas, and the sampling volume  $V = 1.34 \times 10^{-12}$  m<sup>3</sup> corresponding  
 420 to a droplet volume fraction of 0.2 [11].

422 FIG. 7 illustrates the effect of  $m_p/m_d$  on the RSA process (see detailed setups in TA-  
 423 BLE I). The dashed lines represent the jamming state obtained with the assumption of  
 424 an infinite number of particles ( $m_p/m_d = \infty$ ). As  $m_p/m_d$  increases, the number of small  
 425 particles increases. Both  $\phi_j$  and  $\Delta G_d$  increase accordingly and approach the case of infinite  
 426 particles, as shown in FIG. 7(a) and FIG. 7(b). When  $m_p/m_d = 6.53$ ,  $\phi_j$  and  $\Delta G_d$  are only  
 427 1% lower than the case of infinite particles.

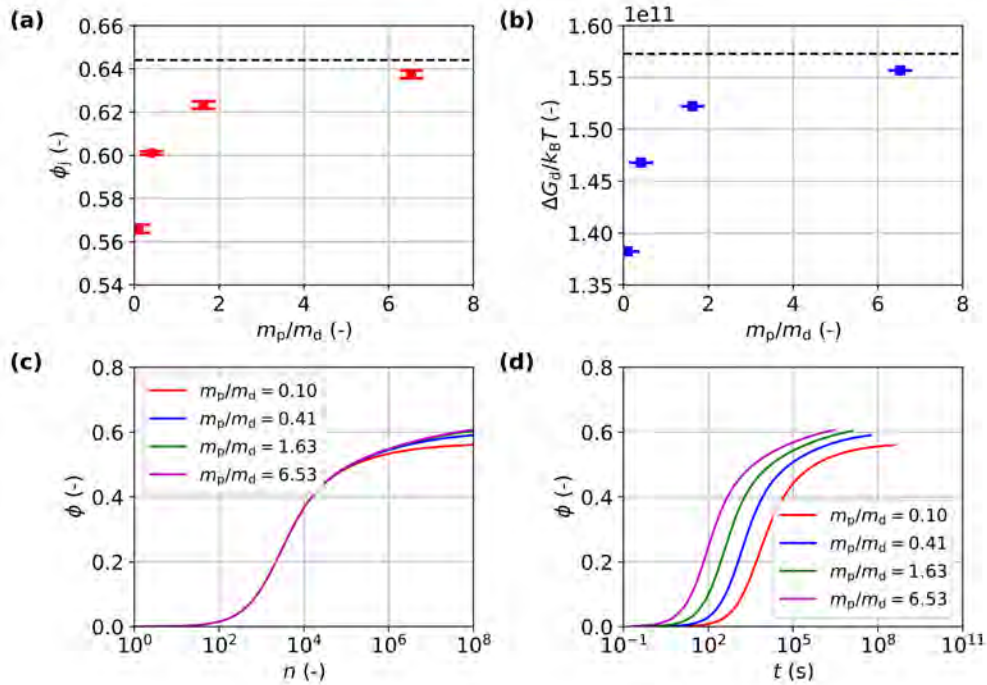


FIG. 7. The effect of emulsion droplet–particle mass ratio,  $m_p/m_d$ , on (a)  $\phi_j$ , (b)  $\Delta G_d/k_B T$ , (c)  $\phi$  evolution with the number of attempts  $n$ , and (d)  $\phi$  evolution with physical time.

428 FIG. 7(c) and FIG. 7(d) show the evolution of  $\phi$  with the number of attempts  $n$  and the  
 429 physical time  $t$ , respectively. When  $n \leq 1 \times 10^5$ , the trends for  $\phi(n)$  are almost identical.  
 430 When  $n > 1 \times 10^5$ , the trends for  $\phi(n)$  present slight differences because a larger  $m_p/m_d$  pro-  
 431 vides more small particles available for adsorption. For the temporal evolution,  $\phi(t)$ , a larger  
 432  $m_p/m_d$  increases the collision frequency and thus decreases the temporal interval between  
 433 two attempts. Consequently, the coverage increases faster for larger values of  $m_p/m_d$ .

434 In addition, the Brownian kernel predicts a much slower adsorption process than that  
 435 in the experiment [11], taking days to reach a moderate coverage (e.g.,  $\phi = 0.5$ ). For

436 Pickering emulsions prepared with high shear mixers, turbulent kernels are the appropriate  
 437 choice and can reproduce experimental time scales if the turbulent flow field and empirical  
 438 constants are available. However, reproducing absolute time scales is not the aim here. Our  
 439 goal is to isolate how particle concentration (via  $m_p/m_d$ ) affects the temporal evolution of  
 440 coverage. Both Brownian and turbulent kernels yield the same relative trend, increasing  
 441  $m_p/m_d$  accelerates coverage growth (see Fig. S3 in the Supplemental Material [64]). The  
 442 Brownian kernel also avoids the need to determine turbulence fields and tune empirical  
 443 constants. Therefore, we use the Brownian kernel to map  $n$  to  $t$  for trend analysis, not to  
 444 reproduce absolute time scales.

445 FIG. 8 illustrates the size distributions of the adsorbed particles and the remaining par-  
 446 ticles at the jamming state. Increasing  $m_p/m_d$  provides more small particles for adsorption.  
 447 Consequently, the skewness towards small sizes of the size distribution of the adsorbed par-  
 448 ticles becomes significant, as shown in FIG. 8(a). The adsorption process’s preference for  
 449 small particles can also be observed in the size distribution of remaining not adsorbed par-  
 450 ticles, as illustrated in FIG. 8(b). When  $m_p/m_d$  is small, for example,  $m_p/m_d = 0.10$ ,  
 451 the smaller particles are completely adsorbed, leading to a zero fraction for particles with  
 452  $r_p \leq 0.92 \mu\text{m}$ .

## 453 2. Generalized coverage evolution model for spherical particles

454 As discussed in previous sections, the key factors influencing the RSA process for spherical  
 455 particles with a normal size distribution are the particle size distribution polydispersity  $CV$ ,  
 456 the emulsion droplet–particle radius ratio  $r_d/r_p$ , and the particle–emulsion droplet mass ratio  
 457  $m_p/m_d$ . Therefore, these parameters were selected as the input variables for the second-  
 458 order response surface models. Their respective selected ranges, summarized in TABLE II,  
 459 were determined with reference to our previous experimental work [11].

460 As described in Section IIC, the LHS generated 21 training conditions (S01 to S21)  
 461 for the three influencing factors, and the CCD generated 8 validation conditions (ST01 to  
 462 ST08). They are listed in TABLE S1 and TABLE S3 of the Supplemental Material [73],  
 463 respectively. Because  $ASF(\phi)$  plays an important role in the coverage evolution model, the  
 464 three fitting expressions (Eq. (11) to Eq. (13)) were evaluated first. Among the parameters  
 465 of  $ASF(\phi)$ ,  $\phi_j$  was obtained using the voxel method, while the remaining ones were fitted

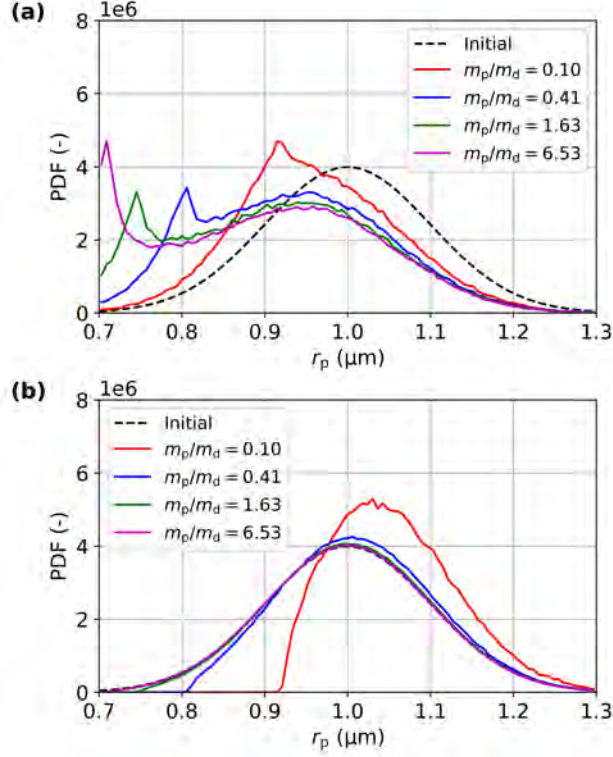


FIG. 8. The size distribution of (a) the adsorbed particles and (b) the remaining particles at the jamming state.

TABLE II. The ranges of three key influencing factors for the RSA process of polydisperse spherical particles.

Factors	Minimum	Maximum
$CV$ (-)	0.01	0.25
$r_d/r_p$ (-)	10	60
$m_p/m_d$ (-)	0.10	1.63

466 to the training dataset. Additionally, two fitting strategies were adopted for the proposed  
 467 Fit 3 to capture the asymptotic behavior better:

- 468 1. Fit 3.1: a constrain,  $e_2 \geq 2$ , is adopted;
- 469 2. Fit 3.2: a fixed  $e_2 = 2.2682$ , which is the mean of  $e_2$  obtained by Fit 3.1, is adopted.

470 The performance of  $ASF(\phi)$  fitting expressions was evaluated by coupling each with the  
 471 coverage evolution model to predict the coverage evolution under the training conditions.

472 For clarity, only the case showing the largest error for Fit 3.1 (case S06 with error of 2.40%)  
 473 is illustrated in FIG. 9(a). Results for the remaining cases are provided in the Supplemental  
 474 Material: FIG. S7 shows coverage evolution, and TABLE S2 summarizes  $R^2$  and MAPE  
 475 [73].

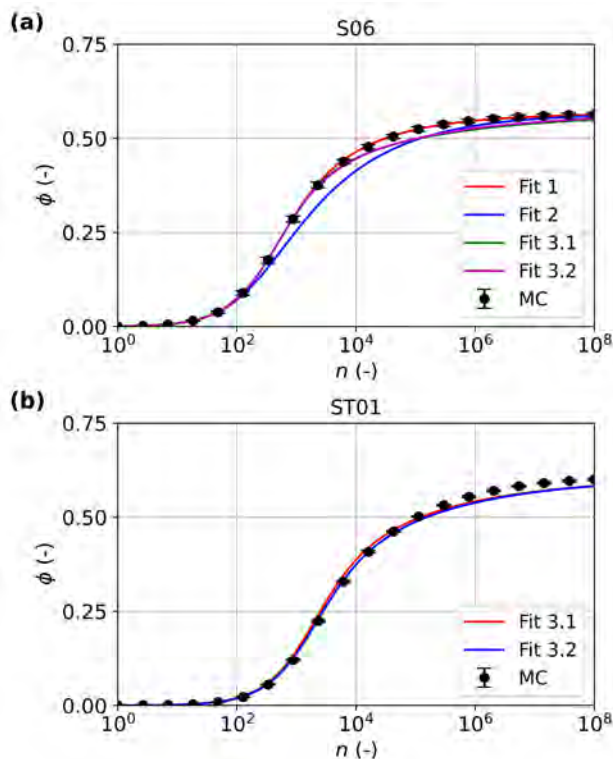


FIG. 9. Coverage evolution predicted by the coverage evolution models and MC simulations: (a) comparison of fitting expressions under the training condition, and (b) validation of the generalized coverage evolution model under the validation condition.

476 For polydisperse particles, the average size of adsorbed particles decreases as the jamming  
 477 state is approached (see Section III A 1), producing a steeper decline in  $ASF(\phi)$ . Due to  
 478 its coverage-dependent exponent, Fit 3 captures this behavior better than Fit 1 and Fit 2.  
 479 Therefore, Fit 2 shows the poorest agreement with MC results, systematically underpredict-  
 480 ing  $ASF(\phi)$  at low coverage ( $\phi \leq 0.5$ ), as shown in the comparison of fittings for  $ASF(\phi)$   
 481 in the Supplemental Material (FIG. S6 [73]). Moreover, Fit 3.1 outperforms Fit 1 in 13  
 482 out of 21 cases (TABLE S2 [73]). Fit 3.2, fixing its parameter  $e_2$ , is comparable to Fit 3.1,  
 483 outperforming Fit 3.1 in 9 out of 21 cases and matching it in 1 case. The standard deviation  
 484 of  $e_2$  from Fit 3.1 is 0.1420, indicating limited variability and justifying the use of a fixed

485 exponent in Fit 3.2 without significant loss in accuracy.

486 Therefore, the proposed Fit 3 provides the best agreement with MC simulations and  
 487 is therefore adopted for estimating  $ASF(\phi)$  in the generalized coverage evolution model  
 488 throughout this study.

489 The generalized coverage evolution model was constructed by regressing the fitted  
 490  $ASF(\phi)$  parameters against the training conditions. The regression  $R^2$  and MAPE are  
 491 summarized in TABLE III. For Fit 3.1, the regression poorly captures the variability of  
 492  $e_2$ , which also degrades the fits for  $e_1$  and  $e_3$ . In contrast, fixing  $e_2$  in Fit 3.2 remarkably  
 493 improves the regressions for  $e_1$  and  $e_3$ .

TABLE III.  $R^2$  and MAPE of the second-order response surface models for  $ASF(\phi)$  parameters in the RSA process of spherical particles.

Parameters	Fit 3.1		Fit 3.2	
	$R^2$	MAPE	$R^2$	MAPE
$e_1$ (-)	0.7926	3.47%	0.9532	1.00%
$e_2$ (-)	0.4209	3.73%	-	-
$e_3$ (-)	0.7603	16.00%	0.9269	5.00%
$\phi_j$ (-)	0.9657	0.50%	0.9657	0.50%

494 The generalized coverage evolution model was then validated against the validation con-  
 495 ditions. For brevity, only case ST01 with the largest error of 2.63% for Fit 3.2 is shown in  
 496 FIG. 9(b). The remaining results are provided in the Supplemental Material (FIG. S8 [73]).  
 497 Both Fit 3.1 and Fit 3.2 provide good agreement with the MC simulations among all cases.  
 498 Fit 3.2, having improved fitting quality for  $e_1$  and  $e_2$  by fixing  $e_2$ , outperforms Fit 3.1 in 6  
 499 out of the 8 cases (TABLE S3 [73]). Detailed second-order response surface equations for  
 500 Fit 3.2 parameters are provided in the Supplemental Material (Eq. (S22) to Eq. (S25) [73]).

501 In summary, the proposed expression (Eq. (13)) provides a more accurate representation  
 502 of  $ASF(\phi)$  because of its coverage-dependent exponent. Based on this, the generalized cov-  
 503 erage evolution model constructed using second-order response surface models is proven to  
 504 be reliable for predicting droplet coverage evolution during the Pickering particle adsorption  
 505 process.

506 **IV. ADSORPTION OF CAPSULE-SHAPED PARTICLES**

507 In this section, the RSA process of monodisperse and polydisperse capsule-shaped par-  
 508 ticles onto spherical droplet surfaces is investigated. The effects of particle polydispersity,  
 509 aspect ratio, particle length, and particle number on the adsorption process were studied.  
 510 The corresponding structures of emulsion droplets with adsorbed particles are presented. A  
 511 generalized coverage evolution model to describe the adsorption for capsule-shaped particles  
 512 is developed. TABLE IV summarizes the setups.

TABLE IV. The MC simulation setups for capsule-shaped particles.

Variables <sup>a</sup>	Monodisperse	Polydisperse ( $\sim \mathcal{N}(\mu, \sigma^2)$ )			
		Polydispersity	Aspect ratio	Length	Particle number <sup>b</sup>
$r_p$ ( $\mu\text{m}$ )	1	-	-	-	-
$\mu_X$ ( $\mu\text{m}$ )	-	5	5	2.5, 5, 10	5
$CV$ (-)	-	0.05, 0.1, 0.2	0.1	0.1	0.1
$m_p/m_d$ (-)	$\infty$	$\infty$	$\infty$	$\infty$	0.1, 0.41, 1.63
$r_d$ ( $\mu\text{m}$ )	40	30	30	30	30
$\theta$ ( $^\circ$ )	90	90	90	90	90
$\epsilon$ (-)	1.1, 2, 4, 8, 12, 16	5	2.5, 5, 10	5	5

<sup>a</sup>  $\mu_X$  is the mean capsule particle length,  $CV = \sigma_X/\mu_X$  is the coefficient of variation of the capsule particle length distribution,  $r_d$  and  $m_d$  are the emulsion droplet radius and mass,  $r_p$  and  $m_p$  are the capsule particle radius and mass,  $\theta$  is the contact angle, and  $\epsilon$  is the capsule particle aspect ratio.

<sup>b</sup> Particle number measured by the particle–emulsion droplet mass ratio  $m_p/m_d$ .

513 **A. Monodisperse particles**

514 FIG. 10 illustrates the effect of aspect ratio  $\epsilon$  of monodisperse capsule-shaped particles  
 515 on the evolutions of  $N_{\text{ad}}$  and  $\phi$ , as well as on the particle packing pattern. As given by  
 516 TABLE IV, the particle diameter  $d_p$  is fixed and particle length  $l_p$  changes with varying  
 517  $\epsilon$ . The increasing  $\epsilon$  leads to longer particles, which occupy larger droplet surface area and  
 518 reduce  $N_{\text{ad}}$  significantly as shown in FIG. 10(a).

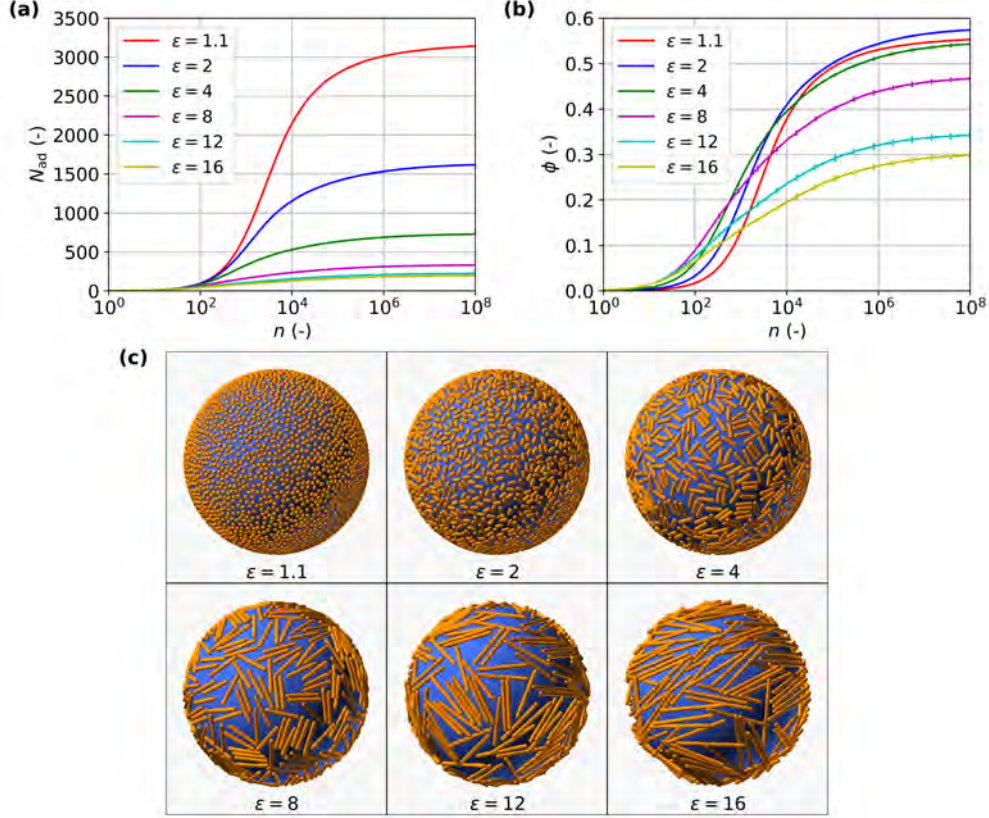


FIG. 10. The effect of aspect ratio  $\epsilon$  of monodisperse capsule-shaped particles on (a) the evolution of  $N_{\text{ad}}$ , (b) the evolution of  $\phi$ , and (c) the particle packing pattern on emulsion droplet surfaces at  $n = 1 \times 10^8$ .

519 FIG. 10(b) illustrates the evolution of  $\phi$ . At the end of the simulation ( $n = 1 \times 10^8$ ),  
 520  $\epsilon = 2$  presents the highest coverage, and  $\epsilon = 1.1$  gives the second highest coverage. Then,  
 521 the coverage decreases with increasing  $\epsilon$ . Similar results were found by Ref. [25], where  
 522  $\epsilon = 1.46$  gave the maximum jamming coverage.

523 This phenomenon results from the competing effects of particle aspect ratio  $\epsilon$  on single-  
 524 particle coverage  $\phi_{\text{p,cap}}$  and exclusion zone. TABLE V gives  $\phi_{\text{p,cap}}$ ,  $N_{\text{ad}}$  and  $\phi$  at  $n = 1 \times 10^8$ .  
 525 Here,  $\epsilon_{\text{crt}} = 9.83$  is the critical aspect ratio. When  $\epsilon \leq \epsilon_{\text{crt}}$ , the semi-spherical parts of the  
 526 adsorbed particles are partially inside the droplet surface, and  $\phi_{\text{p,cap}}$  increases with  $\epsilon$ . When  
 527  $\epsilon > \epsilon_{\text{crt}}$ , the semi-spherical parts of the particles are completely outside the droplet surface,  
 528 and  $\phi_{\text{p,cap}}$  remains a constant. The values of  $\phi_{\text{p,cap}}$  affect the exclusion zone and thus the  
 529 evolution of  $N_{\text{ad}}$  and  $\phi$ .

530 To illustrate the effect of  $\epsilon$ , consider the cases of  $\epsilon = 1.1$  and  $\epsilon = 2$ . When  $\epsilon$  increases

531 from 1.1 to 2,  $\phi_{p,\text{cap}}$  increases by a factor of 2.02, while  $N_{\text{ad}}$  decreases by only a factor of  
 532 0.52. The product of the two factors exceeds one, indicating that the increment in  $\phi_{p,\text{cap}}$   
 533 outweighs the reduction in  $N_{\text{ad}}$  caused by the expanding exclusion zone. Consequently,  $\epsilon = 2$   
 534 results in a higher  $\phi$  compared to  $\epsilon = 1.1$ , when  $n = 1 \times 10^8$ .

TABLE V. The coverage of a single particle,  $\phi_{p,\text{cap}}$ , the number of adsorbed particles,  $N_{\text{ad}}$ , and the coverage,  $\phi$ , under different aspect ratios at  $n = 1 \times 10^8$ .

$\epsilon$ (-)	$\phi_{p,\text{cap}}$ (-)	$N_{\text{ad}}$ (-)	$\phi$ (-)
1.1	$1.76 \times 10^{-4}$	$3140.14 \pm 13.22$	$0.5529 \pm 0.0023$
2	$3.55 \times 10^{-4}$	$1617.52 \pm 7.87$	$0.5739 \pm 0.0028$
4	$7.47 \times 10^{-4}$	$726.63 \pm 6.19$	$0.5431 \pm 0.0046$
8	$1.41 \times 10^{-3}$	$330.26 \pm 3.37$	$0.4668 \pm 0.0048$
12	$1.54 \times 10^{-3}$	$222.48 \pm 5.36$	$0.3424 \pm 0.0083$
16	$1.54 \times 10^{-3}$	$193.94 \pm 4.99$	$0.2985 \pm 0.0077$

535 When  $\epsilon \geq 4$ , the expansion of the exclusion zone overwhelms the increment in  $\phi_{p,\text{cap}}$ . As a  
 536 result,  $\phi$  at  $n = 1 \times 10^8$  monotonically decreases with  $\epsilon$ . Since these cases have reached a near  
 537 jamming state, the jamming coverage  $\phi_j$  obeys the above observations of  $\phi$  at  $n = 1 \times 10^8$ .

538 Additionally, when  $\epsilon \leq 8$ , the increase in  $\epsilon$  leads to a faster coverage change rate at  
 539 the beginning of the adsorption process ( $n \leq 1000$ ). In this condition, the probability of  
 540 successful particle adsorption is high, and the evolution curves of  $N_{\text{ad}}$  are nearly identical.  
 541 Consequently, particles of larger  $\epsilon$  have larger  $\phi_{p,\text{cap}}$  and thus faster coverage change rate.  
 542 This explains the experimental results of Ref. [74]. They adopted particles with aspect  
 543 ratios ranging from 1 to 6 and found that increasing the aspect ratio is an efficient manner  
 544 to stabilize the interface at the same low particle loading. When  $\epsilon > 8$ , the coverage change  
 545 rate decreases with further increasing  $\epsilon$ . This is caused by the constant  $\phi_{p,\text{cap}}$  and decreasing  
 546  $N_{\text{ad}}$ .

547 In summary, a higher jamming coverage  $\phi_j$  or a faster coverage change rate can be ob-  
 548 tained by adjusting the aspect ratio  $\epsilon$  within a suitable range, namely,  $1 < \epsilon < \epsilon_{\text{crt}}$ .

549 FIG. 10(c) illustrates the particle packing pattern on emulsion droplet surfaces with  
 550 varying  $\epsilon$ . As  $\epsilon$  increases, the capsule-shaped particles become longer. When  $\epsilon > \epsilon_{\text{crt}}$ , the  
 551 semi-spherical parts of the particles are completely outside the droplet surface. This may

552 lower the stability of the Pickering emulsions. Additionally, local alignment is observed,  
 553 where particles tend to align their orientations with those of nearby particles. For instance,  
 554 when  $\epsilon = 4$ , the particles exhibit pronounced parallel alignment with their neighboring  
 555 particles. This is also observed in experiments, as shown in FIG. 1.

556 A pair correlation function,  $\eta_{\text{cap}}(r)$ , is adopted to measure this local alignment. Let  $\mathbf{n}_0$   
 557 be the unit vector for the center line of a capsule-shaped particle, and  $r$  is the distance to  
 558 its center. Within the area of  $[r, r + dr]$ , there are  $N_r$  adsorbed particles. The  $i$ th particle  
 559 among them has the unit vector for the center line  $\mathbf{n}_{r,i}$ , where  $i = 1, 2, \dots, N_r$ .  $\eta_{\text{cap}}(r)$  is  
 560 calculated as:

$$\eta_{\text{cap}}(r) = \frac{\sum_{i=1}^{N_r} \arccos(\mathbf{n}_0 \cdot \mathbf{n}_{r,i})}{N_r}, \quad (17)$$

561 where  $r$  increases from 0 to  $2r_d = 80 \mu\text{m}$  with  $dr = 0.4 \mu\text{m}$ .

562 FIG. 11 shows the evolution of  $\eta_{\text{cap}}$  with  $r$  normalized by  $l_p$ .  $l_p$  increases with  $\epsilon$ , the  
 563 curves of larger  $\epsilon$  ends earlier due to the upper bound of  $2r_d/l_p$ . For particles with different  
 564  $\epsilon$ ,  $\eta_{\text{cap}}$  increases from  $0^\circ$  to  $90^\circ$  as  $r/l_p$  increases, and the corresponding curves for different  
 565  $\epsilon$  values almost coincide.

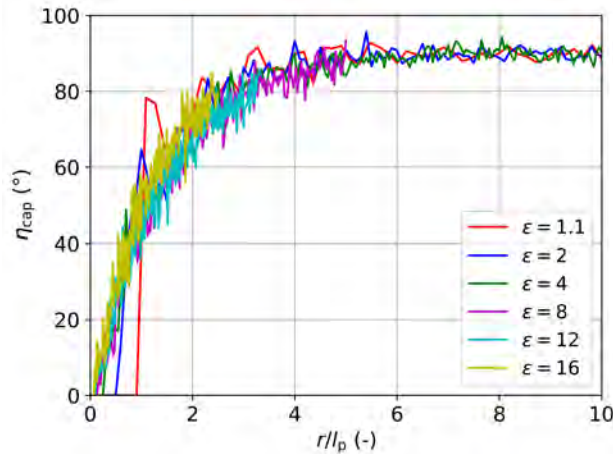


FIG. 11. The pair correlation function  $\eta_{\text{cap}}(r)$  of monodisperse capsule-shaped particles with different aspect ratio  $\epsilon$ .

566 Local alignment makes a selected particle and its near neighbors, those located within  
 567 a small  $r$ , closely oriented in a nearly parallel way. Therefore,  $\eta_{\text{cap}}$  is around zero. When  
 568  $r/l_p \geq 5$ ,  $\eta_{\text{cap}}$  reaches  $90^\circ$ , indicating that particles become randomly oriented and local  
 569 alignment disappears. The orientation of a selected particle no longer influences those of

570 the particles in the area of  $r/l_p \geq 5$ . Instead, their orientations only depend on the uniform  
 571 distribution  $\mathcal{U}[0, 2\pi]$  from which they are generated. Therefore,  $\eta_{\text{cap}}(r)$  fluctuates around  
 572  $90^\circ$ , which corresponds to the expected angle between two randomly oriented capsule-shaped  
 573 particles.

## 574 B. Polydisperse particles

575 FIG. 12 shows the effect of polydispersity, aspect ratio, mean particle length, and particle-  
 576 emulsion droplet mass ratio on coverage evolution and particle packing pattern obtained  
 577 from the MC simulations. Similar to the case of spherical particles, increasing polydispersity  
 578 ( $CV$ ) of the particle size distribution introduces smaller particles that fill the spaces between  
 579 previously adsorbed larger ones, as shown in FIG. 12(b). Consequently,  $\phi$  at  $n = 1 \times 10^8$   
 580 increases, as illustrated in FIG. 12(a).

581 FIG. 12(c) and FIG. 12(d) show the effects of aspect ratio  $\epsilon$  on the coverage evolution  
 582 and particle packing pattern, respectively. In this case, the particle length  $l_p$  follows a nor-  
 583 mal distribution  $\mathcal{N}(\mu, \sigma^2)$ . Increasing  $\epsilon$  decreases particle diameter  $d_p$ , producing narrower  
 584 particles with smaller single-particle coverage  $\phi_{p,\text{cap}}$ , as shown in FIG. 12(d). Consequently,  
 585 FIG. 12(c) shows that increasing  $\epsilon$  slows the coverage growth.

586 When  $\epsilon$  is fixed and the mean particle length increases, the particles become both longer  
 587 and thicker (FIG. 12(f)), leading to a higher  $\phi_{p,\text{cap}}$  and a faster coverage increase (FIG. 12(e)).

588 Finally, FIG. 12(g) and FIG. 12(h) illustrate the effect of particle concentration, rep-  
 589 resented by  $m_p/m_d$ . Although the differences are small in FIG. 12(h), the case with  
 590  $m_p/m_d = 1.63$  adsorbs  $N_{\text{ad}} = 1559$  particles at  $n = 1 \times 10^8$ , about 11.9% more than  
 591 the case with  $m_p/m_d = 0.10$ , resulting in a slightly higher coverage in FIG. 12(g).

## 592 C. Generalized coverage evolution model for capsule-shaped particles

593 This section develops a generalized coverage evolution model for the adsorption of capsule-  
 594 shaped particles with lognormal size distributions. MC simulations for the RSA process  
 595 of capsule-shaped particles are more computationally intensive. Moreover, the objective of  
 596 this study is to demonstrate the framework for constructing a generalized coverage evolution  
 597 model using response surface methodology. Therefore, only two influencing factors, particle

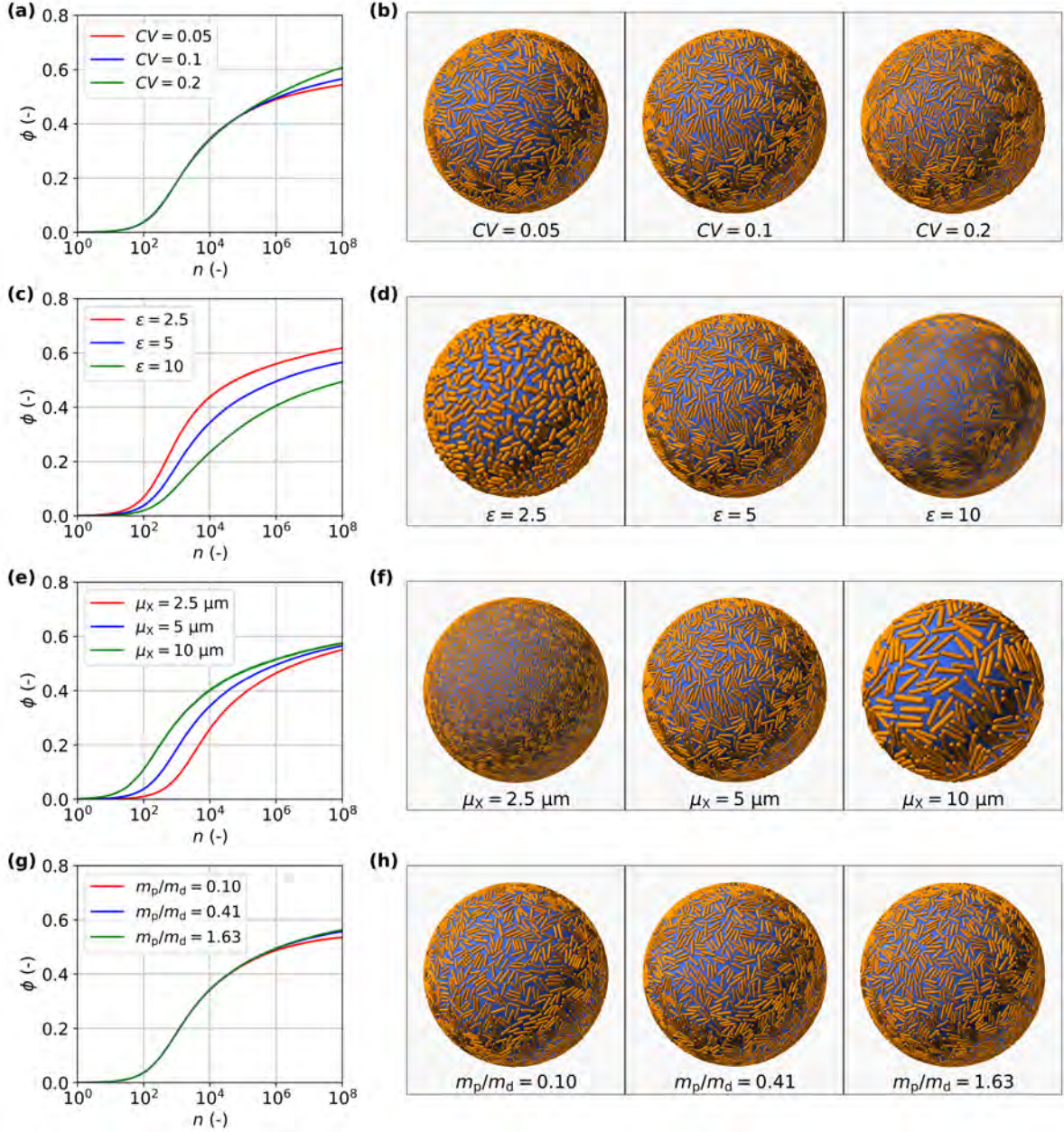


FIG. 12. The coverage evolution and particle packing pattern (at  $n = 1 \times 10^8$ ) for polydisperse capsule-shaped particles under varying conditions: (a) and (b) for coefficient of variation  $CV$ , (c) and (d) for aspect ratio  $\epsilon$ , (e) and (f) for mean particle length  $\mu_X$ , (g) and (h) for particle–emulsion droplet mass ratio  $m_p/m_d$ .

598 polydispersity  $CV$  and emulsion droplet–particle size ratio  $r_d/l_p$ , were considered. Their  
 599 respective ranges are summarized in TABLE VI with reference to findings of our previous  
 600 works [11]. The particle–emulsion droplet mass ratio  $m_p/m_d$  was fixed at 1, which ensures

601 a sufficient number of particles for the RSA process.

TABLE VI. The ranges of two key influencing factors for the RSA process of polydisperse capsule-shaped particles.

Factors	Minimum	Maximum
$CV$ (-)	0.01	0.5
$r_d/l_p$ (-)	10	60

602 As outlined in Section IIC, the LHS generated 15 training conditions (C01 to C15), and  
 603 the CCD generated 6 validation conditions (CT01 to CT06). They are detailed in TABLE S4  
 604 and TABLE S6 of the Supplemental Material [73], respectively. Fit 3.1 and Fit 3.2 were  
 605 used for  $ASF(\phi)$  due to their good accuracy (Section IIIB2). For capsule-shaped particles,  
 606 the jamming coverage  $\phi_j$  was treated as a fitted parameter, which increases the fitting  
 607 complexity. To improve fitting quality, a weighted least-squares method [71] was applied by  
 608 assigning higher weights to high-coverage points ( $\phi \geq 0.5$ ) to better fit  $\phi_j$ .

609 The performance of Fit 3.1 and Fit 3.2 was evaluated for capsule-shaped particles under  
 610 the training conditions. Fit 3.2 fixed its parameter  $e_2$  to 3.5747, the mean  $e_2$  of Fit 3.1.  
 611 For clarity, only case C08, the one with the largest error of 3.90% for Fit 3.1, is shown  
 612 in FIG. 13(a). Results for all remaining cases are provided in the Supplemental Material:  
 613 FIG. S9 for coverage evolution and TABLE S5 for  $R^2$  and MAPE [73]. To avoid inflated  
 614 MAPE values at low coverage, only data points with  $\phi \geq 0.1$  are included in the calculation.  
 615 This threshold is reasonable, as most of the simulated attempts occur within this coverage  
 616 range.

617 Overall, Fit 3.1 outperforms Fit 3.2 in 8 of the 15 cases and performs equally well in  
 618 one case (see TABLE S5 [73]). The slightly reduced performance of Fit 3.2 arises from the  
 619 larger variability of  $e_2$  in Fit 3.1 (standard deviation 0.7077), indicating that fixing  $e_2$  across  
 620 all cases can compromise fitting accuracy. For example, in case C08,  $e_2 = 2.1388$  in Fit 3.1  
 621 deviates significantly from the fixed mean value used in Fit 3.2, leading to a less accurate  
 622 prediction by the coverage evolution model.

623 The generalized coverage evolution was constructed by regressing the fitted  $ASF(\phi)$  pa-  
 624 rameters against the training conditions, with regression  $R^2$  and MAPE summarized in  
 625 TABLE VII. Consistent with the case of spherical particles, fixing  $e_2$  in Fit 3.2 improves the

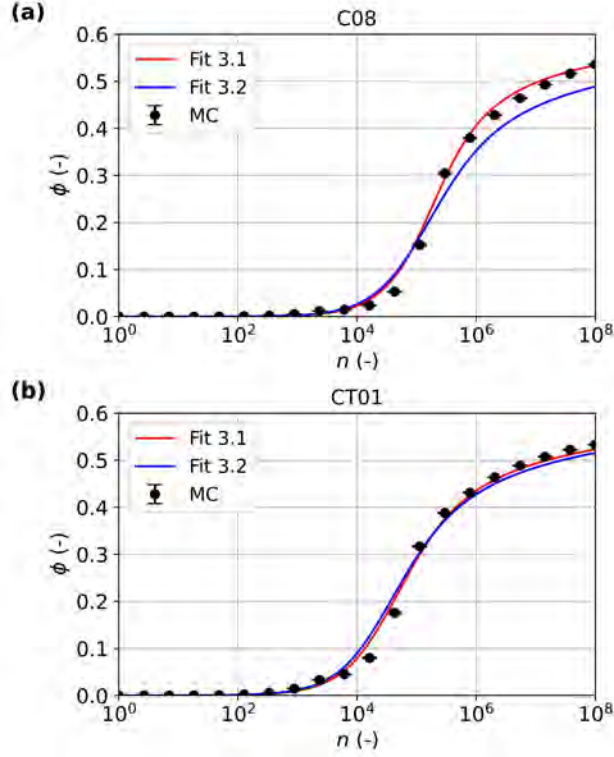


FIG. 13. Coverage evolution predicted by the coverage evolution models and MC simulations: (a) comparison of fitting expressions under the training condition, and (b) validation of the generalized coverage evolution model under the validation condition.

626 fitting quality for both  $e_1$  and  $e_2$ . However, the fitting quality of all parameters in Fit 3.1  
 627 remains acceptable, indicating that it can still capture the underlying trends.

TABLE VII.  $R^2$  and MAPE of the second-order response surface models for  $ASF(\phi)$  parameters in the RSA process of capsule-shaped particles.

Parameters	Fit 3.1		Fit 3.2	
	$R^2$	MAPE	$R^2$	MAPE
$e_1 (-)$	0.8755	11.10%	0.9471	3.65%
$e_2 (-)$	0.8724	5.68%	-	-
$e_3 (-)$	0.7695	16.02%	0.9191	12.01%
$\phi_j (-)$	0.9900	0.53%	0.9900	0.53%

628 Finally, the generalized coverage evolution model was validated on the validation condi-

629 tions. For brevity, only case CT01, the one showing the largest error of 6.58% for Fit 3.1,  
 630 is shown in FIG. 13(b). The remaining results are provided in the Supplemental Material  
 631 (FIG. S10 for coverage evolution and TABLE S6 for  $R^2$  and MAPE [73]). Overall, model  
 632 predictions agree well with the MC simulations. Fit 3.1, which allows  $e_2$  to vary, outper-  
 633 forms Fit 3.2 in 5 of the 6 validation cases, indicating that Fit 3.1 provides a more accurate  
 634 representation of  $ASF(\phi)$  for polydisperse, anisotropic capsule-shaped particles. The de-  
 635 tailed second-order response surface expressions for Fit 3.1 parameters are provided in the  
 636 Supplemental Material (Eq. (S26) to Eq. (S29) [73]).

637 In summary, the generalized coverage evolution model based on Fit 3.1 proves effective  
 638 in capturing the RSA process of capsule-shaped particles across a wide range of conditions,  
 639 offering a reliable predictive framework for future applications.

## 640 V. CONCLUSIONS

641 Micron-sized, crystalline particles have received increasing attention for stabilizing Pick-  
 642 ering emulsions. Due to their larger sizes, the effects of the curvature and the finite size of  
 643 spherical emulsion droplet surfaces should be considered to describe interfacial adsorption.  
 644 This study investigates the random sequential adsorption (RSA) of micron-sized particles  
 645 onto spherical surfaces from both low-coverage and asymptotic perspectives. Isotropic spher-  
 646 ical particles and anisotropic capsule-shaped particles were considered. A Monte Carlo (MC)  
 647 method was employed to simulate the RSA process, systematically exploring the effects of  
 648 several factors. A new expression of the available surface function,  $ASF(\phi)$ , was proposed  
 649 and compared with those from the literature. Based on this, a generalized coverage evolu-  
 650 tion model was constructed by linking key influencing factors of the RSA process to  $ASF(\phi)$   
 651 parameters by the response surface methodology.

652 The effects of curvature and finite size are incorporated by the emulsion droplet–particle  
 653 geometric relationships derived from the spherical emulsion droplet surfaces. Regarding the  
 654 influencing factors in the RSA process of Pickering particles, the jamming coverage,  $\phi_j$ , and  
 655 free energy of particle desorption,  $\Delta G_d$ , increase with particle polydispersity due to the  
 656 larger number of smaller particles. For emulsion droplets produced in the same batch, their  
 657 jamming coverages are almost identical regardless of the emulsion droplet–particle size ratio.  
 658 Increasing the contact angle from  $90^\circ$  to  $150^\circ$  leads to reductions in both  $\phi_j$  and  $\Delta G_d$ , which

659 means lower surface coverage and emulsion stability. A higher particle–emulsion droplet  
660 mass ratio increases  $\phi_j$ , closer to the case of infinite particles. Meanwhile, this also increases  
661 collision frequency and accelerates the adsorption process. In particular, for capsule-shaped  
662 particles, the aspect ratio,  $\epsilon$ , plays an important role. When  $\epsilon$  is larger than a critical  
663 value, the semi-spherical parts of particles are outside of the droplet interfaces and provide  
664 a constant single-particle coverage due to the curvature of droplet interfaces. An aspect  
665 ratio of  $\epsilon = 2$  achieves higher  $\phi_j$  and faster coverage increasing rate. A local alignment,  
666 related to the long axis of capsule-shaped particles, is observed in the simulations. These  
667 findings deepen the understanding of the RSA process in Pickering emulsion production  
668 processes and provide valuable information on  $\phi_j$ , which is essential to predict emulsion  
669 stability, encapsulation efficiency, and API release rate.

670 As for the RSA coverage evolution, a new expression for  $ASF(\phi)$ , with a coverage-  
671 dependent exponent, is proposed, which is more flexible and accurate than the existing  
672 expressions in the literature, using a fixed exponent. Based on this, generalized coverage  
673 evolution models are constructed for spherical and capsule-shaped particles, respectively.  
674 The key influencing factors of RSA processes are linked to the  $ASF(\phi)$  parameters through  
675 second-order response surface models. The validations show that both models work well,  
676 leading to MAPE no larger than 2.63% for spherical particles and 6.58% for capsule-shaped  
677 particles in all validation cases. The generalized coverage evolution models are applicable  
678 across varied conditions and offer an efficient and practical tool to simulate the RSA behavior  
679 of Pickering particles. The presented framework for the construction of the generalized  
680 coverage evolution model can be extended to the RSA process of various kinds of Pickering  
681 emulsion formulations, prepared under various processing conditions. This is an important  
682 tool for the design and optimization of Pickering emulsion production processes, and it  
683 represents an essential step for the construction of a generalized model that describes API  
684 release from Pickering emulsion.

## 685 **ACKNOWLEDGMENTS**

686 This project has received funding from the European Research Council (ERC) under  
687 the European Union’s Horizon 2020 research and innovation program (grant agreement No  
688 949229). PI: Prof. Elena Simone. Computational resources provided by HPC@PoliTO

689 (www.hpc.polito.it). Prof. Marco Vanni is acknowledged for useful discussions on the sam-  
690 pling method of spherical surfaces and the convergence examination of the Monte Carlo  
691 method.

- 
- 692 [1] C. Albert, M. Beladjine, N. Tsapis, E. Fattal, F. Agnely, and N. Huang, Pickering emulsions:  
693 Preparation processes, key parameters governing their properties and potential for pharma-  
694 ceutical applications, *Journal of Controlled Release* **309**, 302 (2019).
- 695 [2] F. Heidari-Dalfard, S. Tavasoli, E. Assadpour, R. Miller, and S. M. Jafari, Surface modification  
696 of particles/nanoparticles to improve the stability of Pickering emulsions; a critical review,  
697 *Advances in Colloid and Interface Science* **336**, 103378 (2025).
- 698 [3] C. Li, Y. Li, P. Sun, and C. Yang, Pickering emulsions stabilized by native starch granules,  
699 *Colloids and Surfaces A: Physicochemical and Engineering Aspects* **431**, 142 (2013).
- 700 [4] G. Frungieri and H. Briesen, A population balance model for the flow-induced preparation of  
701 Pickering emulsions, *Chemical Engineering Research and Design* **189**, 694 (2023).
- 702 [5] B. P. Binks and T. S. Horozov, eds., *Colloidal Particles at Liquid Interfaces*, 1st ed. (Cam-  
703 bridge University Press, 2006).
- 704 [6] Y. Liu and Y. Xi, Colloidal systems with a short-range attraction and long-range repulsion:  
705 Phase diagrams, structures, and dynamics, *Current Opinion in Colloid & Interface Science*  
706 **39**, 123 (2019).
- 707 [7] J. Xu, Y. Liu, T. Guo, G. Sun, J. Luo, R. Liu, Y.-L. Steve Tse, and T. Ngai, Investigation  
708 of the Contact Angle and Packing Density of Silica Nanoparticles at a Pickering Emulsion  
709 Interface Fixed by UV Polymerization, *Langmuir* **38**, 4234 (2022).
- 710 [8] Y. He and X. Yu, Preparation of silica nanoparticle-armored polyaniline microspheres in a  
711 Pickering emulsion, *Materials Letters* **61**, 2071 (2007).
- 712 [9] H. Firoozmand and D. Rousseau, Microbial cells as colloidal particles: Pickering oil-in-water  
713 emulsions stabilized by bacteria and yeast, *Food Research International* **81**, 66 (2016).
- 714 [10] B. P. Binks and S. O. Lumsdon, Pickering Emulsions Stabilized by Monodisperse Latex Par-  
715 ticles: Effects of Particle Size, *Langmuir* **17**, 4540 (2001).
- 716 [11] G. Del Duca, E. Parisi, F. Artusio, E. Cali, S. Fraterrigo Garofalo, C. Rosso, V. Cauda, M. R.  
717 Chierotti, and E. Simone, A crystal engineering approach for rational design of curcumin

- 718 crystals for Pickering stabilization of emulsions, *Food Research International* **194**, 114871  
719 (2024).
- 720 [12] D. Ershov, J. Sprakel, J. Appel, M. A. Cohen Stuart, and J. Van Der Gucht, Capillarity-  
721 induced ordering of spherical colloids on an interface with anisotropic curvature, *Proc. Natl.*  
722 *Acad. Sci. U.S.A.* **110**, 9220 (2013).
- 723 [13] P. Kubala, P. Batys, J. Barbasz, P. Weroński, and M. Cieśla, Random sequential adsorption:  
724 An efficient tool for investigating the deposition of macromolecules and colloidal particles,  
725 *Advances in Colloid and Interface Science* **306**, 102692 (2022).
- 726 [14] J. Feder, Random sequential adsorption, *Journal of Theoretical Biology* **87**, 237 (1980).
- 727 [15] M. Cieśla and J. Barbasz, Random packing of regular polygons and star polygons on a flat  
728 two-dimensional surface, *Phys. Rev. E* **90**, 022402 (2014).
- 729 [16] E. L. Hinrichsen, J. Feder, and T. Jøssang, Geometry of random sequential adsorption, *J Stat*  
730 *Phys* **44**, 793 (1986).
- 731 [17] R. D. Vigil and R. M. Ziff, Random sequential adsorption of unoriented rectangles onto a  
732 plane, *The Journal of Chemical Physics* **91**, 2599 (1989).
- 733 [18] K. Haiduk, P. Kubala, and M. Cieśla, Saturated packings of convex anisotropic objects under  
734 random sequential adsorption protocol, *Phys. Rev. E* **98**, 063309 (2018).
- 735 [19] P. Abritta and R. S. Hoy, Structure of saturated random-sequential-adsorption ellipse pack-  
736 ings, *Phys. Rev. E* **106**, 054604 (2022).
- 737 [20] A. Abbasi Moud, Precise Determination of the Saturation Coverage of Polygons In Silico  
738 Using Exclusion Assisted Packing Technique, *J Stat Phys* **190**, 93 (2023).
- 739 [21] M. Cieśla, P. Kubala, and K. Kozubek, Algorithms to generate saturated random sequential  
740 adsorption packings built of rounded polygons, *Phys. Rev. E* **103**, 063308 (2021).
- 741 [22] M. Cieśla, G. Pająk, and R. M. Ziff, Shapes for maximal coverage for two-dimensional random  
742 sequential adsorption, *Phys. Chem. Chem. Phys.* **17**, 24376 (2015).
- 743 [23] L. Petrone and M. Cieśla, Random sequential adsorption of oriented rectangles with random  
744 aspect ratio, *Phys. Rev. E* **104**, 034903 (2021).
- 745 [24] N. Lebovka, M. Petryk, M. O. Tatchenko, and N. V. Vygornitskii, Two-stage random se-  
746 quential adsorption of discorectangles and disks on a two-dimensional surface, *Phys. Rev. E*  
747 **108**, 024109 (2023).
- 748 [25] N. I. Lebovka, N. V. Vygornitskii, and Y. Y. Tarasevich, Random sequential adsorption of

- 749 partially ordered discorectangles onto a continuous plane, *Phys. Rev. E* **102**, 022133 (2020).
- 750 [26] R. C. Doty, R. T. Bonnecaze, and B. A. Korgel, Kinetic bottleneck to the self-organization of  
751 bidisperse hard disk monolayers formed by random sequential adsorption, *Phys. Rev. E* **65**,  
752 10.1103/physreve.65.061503 (2002).
- 753 [27] P. Danwanichakul and T. Charinpanitkul, Random sequential adsorption of polydisperse  
754 spherical particles: An integral-equation theory, *Physica A: Statistical Mechanics and its  
755 Applications* **377**, 102 (2007).
- 756 [28] N. V. Brilliantov, Yu. A. Andrienko, P. L. Krapivsky, and J. Kurths, Fractal Formation and  
757 Ordering in Random Sequential Adsorption, *Phys. Rev. Lett.* **76**, 4058 (1996).
- 758 [29] Z. Adamczyk, B. Siwek, M. Zembala, and P. Weroński, Influence of Polydispersity on Random  
759 Sequential Adsorption of Spherical Particles, *Journal of Colloid and Interface Science* **185**, 236  
760 (1997).
- 761 [30] R. C. Hart and F. D. A. Aarão Reis, Random sequential adsorption of polydisperse mixtures  
762 on lattices, *Phys. Rev. E* **94**, 022802 (2016).
- 763 [31] P. Viot, G. Tarjus, S. M. Ricci, and J. Talbot, Random sequential adsorption of anisotropic  
764 particles. I. Jamming limit and asymptotic behavior, *The Journal of Chemical Physics* **97**,  
765 5212 (1992).
- 766 [32] G. Zhang and S. Torquato, Precise algorithm to generate random sequential addition of hard  
767 hyperspheres at saturation, *Phys. Rev. E* **88**, 053312 (2013).
- 768 [33] J.-S. Wang, A fast algorithm for random sequential adsorption of discs, *Int. J. Mod. Phys. C*  
769 **05**, 707 (1994).
- 770 [34] G. Zhang, Precise algorithm to generate random sequential adsorption of hard polygons at  
771 saturation, *Phys. Rev. E* **97**, 043311 (2018).
- 772 [35] W. Kasperek, P. Kubala, and M. Cieśla, Random sequential adsorption of unoriented rectan-  
773 gles at saturation, *Phys. Rev. E* **98**, 063310 (2018).
- 774 [36] P. Schaaf and J. Talbot, Kinetics of Random Sequential Adsorption, *Physical Review Letters*  
775 **62**, 175 (1989).
- 776 [37] J. W. Evans, Comment on “Kinetics of random sequential adsorption”, *Physical Review Let-  
777 ters* **62**, 2642 (1989).
- 778 [38] J. W. Evans, Random and cooperative sequential adsorption, *Rev. Mod. Phys.* **65**, 1281 (1993).
- 779 [39] S. M. Ricci, J. Talbot, G. Tarjus, and P. Viot, Random sequential adsorption of anisotropic

- 780 particles. II. Low coverage kinetics, *The Journal of Chemical Physics* **97**, 5219 (1992).
- 781 [40] M. Cieřła and J. Barbasz, Modelling of interacting dimer adsorption, *Surface Science* **612**, 24  
782 (2013).
- 783 [41] V. Tartaglione, C. Farges, and J. Sabatier, Nonlinear dynamical modeling of adsorption and  
784 desorption processes with power-law kinetics: Application to CO<sub>2</sub> capture, *Phys. Rev. E* **102**,  
785 052102 (2020).
- 786 [42] Z. Adamczyk, B. Senger, J.-C. Voegel, and P. Schaaf, Irreversible adsorption/deposition ki-  
787 netics: A generalized approach, *The Journal of Chemical Physics* **110**, 3118 (1999).
- 788 [43] R. Kopelman, Fractal Reaction Kinetics, *Science* **241**, 1620 (1988).
- 789 [44] Y. Ho and G. McKay, The kinetics of sorption of divalent metal ions onto sphagnum moss  
790 peat, *Water Research* **34**, 735 (2000).
- 791 [45] F. Brouers and O. Sotolongo-Costa, Generalized fractal kinetics in complex systems (applica-  
792 tion to biophysics and biotechnology), *Physica A: Statistical Mechanics and its Applications*  
793 **368**, 165 (2006).
- 794 [46] I. Tavernier, W. Wijaya, P. Van Der Meeren, K. Dewettinck, and A. R. Patel, Food-grade  
795 particles for emulsion stabilization, *Trends in Food Science & Technology* **50**, 159 (2016).
- 796 [47] J. Xiao, Y. Li, and Q. Huang, Recent advances on food-grade particles stabilized Pickering  
797 emulsions: Fabrication, characterization and research trends, *Trends in Food Science &*  
798 *Technology* **55**, 48 (2016).
- 799 [48] B. S. Murray, K. Durga, A. Yusoff, and S. D. Stoyanov, Stabilization of foams and emulsions  
800 by mixtures of surface active food-grade particles and proteins, *Food Hydrocolloids* **25**, 627  
801 (2011).
- 802 [49] S. B. Haaaj, W. Thielemans, A. Magnin, and S. Boufi, Starch Nanocrystal Stabilized Pickering  
803 Emulsion Polymerization for Nanocomposites with Improved Performance, *ACS Appl. Mater.*  
804 *Interfaces* **6**, 8263 (2014).
- 805 [50] H.-N. Liang and C.-h. Tang, Pea protein exhibits a novel Pickering stabilization for oil-in-water  
806 emulsions at pH 3.0, *LWT - Food Science and Technology* **58**, 463 (2014).
- 807 [51] J. Wu, M. Shi, W. Li, L. Zhao, Z. Wang, X. Yan, W. Norde, and Y. Li, Pickering emul-  
808 sions stabilized by whey protein nanoparticles prepared by thermal cross-linking, *Colloids and*  
809 *Surfaces B: Biointerfaces* **127**, 96 (2015).
- 810 [52] X. Song, Y. Pei, M. Qiao, F. Ma, H. Ren, and Q. Zhao, Preparation and characterizations

- 811 of Pickering emulsions stabilized by hydrophobic starch particles, *Food Hydrocolloids* **45**, 256  
812 (2015).
- 813 [53] L. A. Rosen, N. A. Seaton, and E. D. Glandt, Random sequential adsorption onto the surface  
814 of small spheres, *The Journal of Chemical Physics* **85**, 7359 (1986).
- 815 [54] E. R. Chen and M. Holmes-Cerfon, Random Sequential Adsorption of Discs on Surfaces of  
816 Constant Curvature: Plane, Sphere, Hyperboloid, and Projective Plane, *J Nonlinear Sci* **27**,  
817 1743 (2017).
- 818 [55] B. M. Manzi, M. Werner, E. P. Ivanova, R. J. Crawford, and V. A. Baulin, Simulations of  
819 Protein Adsorption on Nanostructured Surfaces, *Sci Rep* **9**, 4694 (2019).
- 820 [56] P. Kubala and M. Cieřła, The effect of substrate waviness on random sequential adsorption  
821 packing properties, *J. Stat. Mech.* **2022**, 033303 (2022).
- 822 [57] S. Levine and B. Bowen, Capillary interaction of spherical particles adsorbed on the surface of  
823 an oil/water droplet stabilized by the particles. Part I, *Colloids and Surfaces* **59**, 377 (1991).
- 824 [58] R. Aveyard, J. H. Clint, and T. S. Horozov, Aspects of the stabilisation of emulsions by solid  
825 particles: Effects of line tension and monolayer curvature energy, *Phys. Chem. Chem. Phys.*  
826 **5**, 2398 (2003).
- 827 [59] J. C. Loudet, A. M. Alsayed, J. Zhang, and A. G. Yodh, Capillary Interactions Between  
828 Anisotropic Colloidal Particles, *Phys. Rev. Lett.* **94**, 018301 (2005).
- 829 [60] J. C. Loudet, A. G. Yodh, and B. Pouligny, Wetting and Contact Lines of Micrometer-Sized  
830 Ellipsoids, *Phys. Rev. Lett.* **97**, 018304 (2006).
- 831 [61] (2025), See Supplemental Material at URL for Section S1, which shows the calculation of the  
832 coverage of a single capsule-shaped particle.
- 833 [62] C. Ericson, *Real-Time Collision Detection*, nachdr. ed., Morgan Kaufmann Series in Interactive  
834 3D Technology (Elsevier, Amsterdam Heidelberg, 2004).
- 835 [63] (2025), See Supplemental Material at URL for Section S2, which presents the voxel method  
836 for polydisperse spherical particles.
- 837 [64] (2025), See Supplemental Material at URL for Section S3, which shows the convergence ex-  
838 amination for the Monte Carlo simulation.
- 839 [65] C. Coulaloglou and L. Tavlarides, Description of interaction processes in agitated liquid-liquid  
840 dispersions, *Chemical Engineering Science* **32**, 1289 (1977).
- 841 [66] J. Zhang, S. Xu, and W. Li, High shear mixers: A review of typical applications and studies

- 842 on power draw, flow pattern, energy dissipation and transfer properties, *Chemical Engineering*  
843 *and Processing: Process Intensification* **57–58**, 25 (2012).
- 844 [67] S. Castellano, N. Sheibat-Othman, D. Marchisio, A. Buffo, and S. Charton, Description of  
845 droplet coalescence and breakup in emulsions through a homogeneous population balance  
846 model, *Chemical Engineering Journal* **354**, 1197 (2018).
- 847 [68] M. J. Prince and H. W. Blanch, Bubble coalescence and break-up in air-sparged bubble  
848 columns, *AIChE Journal* **36**, 1485 (1990).
- 849 [69] A. I. Khuri and S. Mukhopadhyay, Response surface methodology, *WIREs Comp Stat* **2**, 128  
850 (2010).
- 851 [70] R. H. Myers, D. C. Montgomery, and C. M. Anderson-Cook, *Response Surface Methodology:*  
852 *Process and Product Optimization Using Designed Experiments*, fourth edition ed., Wiley  
853 Series in Probability and Statistics (Wiley, Hoboken, New Jersey, 2016).
- 854 [71] W. H. Press, S. A. Teukolsky, W. T. Vetterling, and B. P. Flannery, *Numerical Recipes: The*  
855 *Art of Scientific Computing*, 3rd ed. (Cambridge University Press, Cambridge, 2007).
- 856 [72] A. De Myttenaere, B. Golden, B. Le Grand, and F. Rossi, Mean Absolute Percentage Error  
857 for regression models, *Neurocomputing* **192**, 38 (2016).
- 858 [73] (2025), See Supplemental Material at URL for Section S4, which provides the details for  
859 constructing the generalzied kinetic model for spherical and capsule-shaped particles.
- 860 [74] B. Madivala, S. Vandebril, J. Fransaer, and J. Vermant, Exploiting particle shape in solid  
861 stabilized emulsions, *Soft Matter* **5**, 1717 (2009).